A Gamma-Ray Burst Mission to Investigate the Properties of Dark Energy

A White Paper Submitted to the Dark Energy Task Force
15 June 2005

Point of contact: d-lamb@uchicago.edu

D. Q. Lamb[1], G. R. Ricker[2], D. Lazzati[3], G. Ghirlanda[4], G. Ghisellini[4], C. Firmani[4,5], L. Amati[6], J.-L. Atteia[7], V. Avila-Reese[5], S. Burles[2], N. Butler[2], H.-W. Chen[2], E. Costa[8], J. Doty[9], F. Frontera[6], A. Fruchter[10], P. Garnavich[11], C. Graziani[1], J. G. Jernigan[12], N. Kawai[13], P. Mazzali[14], P. Meszaros[15], L. Piro[8], T. Sakamoto[16], K. Stanek[17], M. Vietri[18], M. della Valle[19], J. Villasenor[2], B. Zhang[20]

[1]U. Chicago; [2]MIT; [3]U. Colorado; [4]Osservatorio Astronomico di Brera; [5]U.N.A.M.; [6]IAFSC, sezione Bologna, CNR; [7]Observatoire Midi-Pyrénées; [8]Istituto di Astrofisica Spaziale e Fisica Cosmica – INAF, Roma; [9]Noqsi Aerospace, Ltd.; [10]STScI; [11]U. Notre Dame; [12]UC Berkeley; [13]Tokyo Institute of Technology; [14]Osservatorio Astronomico, Trieste; [15]Penn State; [16]GSFC; [17]CfA; [18]Scuola Normale Superiore, Pisa; [19]Osservatorio Astronomico di Arcetri; [20]UNLV

Executive Summary

Gamma-ray bursts (GRBs) are the most brilliant events in the universe. The intrinsic luminosities of the bursts span more than five decades. At first glance, therefore, these events would hardly seem to be promising standard candles for cosmology. However, very recently, relations between the peak energy $E_{\rm peak}$ of the burst spectrum in νF_ν, the isotropic-equivalent energy $E_{\rm iso}$ of the burst, and the radiated energy E_γ of the burst – all in the rest frame of the burst source – have been found. In a way that is exactly analogous to the way in which the relation between the peak luminosity and the rate of decline of the light curve of Type Ia supernovae can be used to make Type Ia supernovae excellent standard candles for cosmology, so too, the relations between $E_{\rm peak}$, $E_{\rm iso}$, and E_γ point toward a methodology for using GRBs as excellent standard candles for cosmology. In addition, GRBs occur over the broad redshift range from $z = 0.1$ to at least $z = 4.5$, and both they and their afterglows are easily detectable out to $z > 8$. Thus GRBs show great promise as cosmological "yardsticks" to measure the rate of expansion of the universe over time, and therefore the properties of dark energy (i.e., Ω_M, $\Omega_{\rm DE}$, w_0, and w_a).

Measurements of four observational quantities are needed in order to use a GRB as a standard candle": (1) the observed peak energy $E^{\rm obs}_{\rm peak}$ of the burst spectrum in νF_ν (2) the energy fluence S_E of the burst, (3) the jet break time $t_{\rm jet}$ of the burst afterglow, and (4) the redshift z of the burst. We describe a concept for a possible MIDEX-class mission dedicated to using GRBs to constrain the properties of dark energy that would obtain these quantities for > 800 bursts in the redshift range $0.1 \lesssim z \lesssim 10$ during a 2-year mission. This burst sample would enable both Ω_M and w_0 to be determined to ± 0.07 and ± 0.06 (68% CL), respectively, and w_a to be significantly constrained. Probing the properties of dark energy using GRBs is complementary (in the sense of parameter degeneracies) to other probes, such as CMB anisotropies and X-ray clusters. GRBs are complementary to Type Ia supernovae because of the broader redshift range over which GRBs occur, and the ease with which they and their afterglows can be observed.

The MIDEX-class mission concept calls for three small spacecraft placed at L_2 in the Earth-Sun system. One spacecraft, a minisatellite, would carry an array of X-ray CCD cameras very similar to the Soft X-Ray Camera (SXC) on *HETE-2* and a set of large-area NaI detectors. The array of X-ray CCD cameras would have a sensitivity $\sim$ twice that of the Wide-Field X-Ray Monitor (WXM) on *HETE-2* . The field of view (FOV) of the array would be $\approx 2\pi$ steradians, $10\times$ greater than that of the WXM. It would localize bursts to $\approx 1''$accuracy. The set of NaI detectors, combined with the array of X-ray CCD cameras, would determine $E^{\rm obs}_{\rm peak}$ and S_E to 10% accuracy (90% CL) over the 1–1000 keV energy range. The other two spacecraft–both microsatellites– would carry identical, high throughput, short (80 cm) focal length X-ray telescopes for monitoring the X-ray afterglows of each of the bursts and determining $t_{\rm jet}$ for them. The mission concept incorporates six dedicated, ground-based 2-meter class telescopes with integral field spectrographs (IFS) distributed in longitude around the Earth for promptly observing the optical afterglows of the bursts and determining their redshifts.

1. Precursor Observations

Recently, Amati et al. (2002) discovered a relation between the peak energy $E_{\rm peak}$ of the burst spectrum in νF_ν and the isotropic-equivalent energy $E_{\rm iso}$ of the burst in the source rest frame, using 10 *Beppo*SAX GRBs with known redshifts. Lamb et al. (2004; see also Sakamoto et al. 2004, 2005) confirmed this relation for GRBs and found evidence that it extends down to X-ray-rich GRBs (XRRs) and X-Ray Flashes (XRFs) and therefore spans five decades in $E_{\rm iso}$,

Very recently, Ghirlanda et al. (2004a) provided further confirmation of this relation and discovered that an even tighter relation exists between $E_{\rm peak}$ and E_γ, where $E_\gamma \equiv (1-\cos\theta_{\rm jet})E_{\rm iso}$ (see Figure 1), where $\theta_{\rm jet}$ is inferred from the jet break time $t_{\rm jet}$. Still more recently, Liang & Zhang (2005) have shown that an equally tight relation exists directly among $E_{\rm peak}$, $E_{\rm iso}$, and $t_{\rm jet}$, which places the $E_{\rm peak} - E_\gamma$ relation on an entirely empirical footing.

Using the $E_{\rm peak} - E_\gamma$ relation, Ghirlanda et al. (2004b) and Firmani et al. (2005) have shown that GRBs can be used as standard candles for cosmology. In, particular, they have shown that the uncertainty in $E_{\rm iso}$ using this method is currently about 0.25 dex, which is only twice the current uncertainty in the luminosities L_{SN} of Type Ia supernovae (SNe) after using the analogous relation between L_{SN} and the rate of decline of the SN light curves Riess et al. (2004). These results suggest that, although the use of GRBs as standard candles is less than a year old, while the use of Type Ia SNe is more than a half century old, GRBs hold great promise for cosmology. GRBs are also complementary to Type Ia SNe because of the broad redshift range over which GRBs occur, and the ease with which they and their afterglows can be observed.

The "Gold" GRB sample used by Ghirlanda et al. (2004; see also Ghisellini et al. 2005 and Firmani et al. 2005) consists of 15 GRBs for which $E_{\rm peak}$, $E_{\rm iso}$, $t_{\rm jet}$, and z are well determined. Ghirlanda et al. (2004b) and Firmani et al. (2005) show that, using this small sample of GRBs, interesting constraints can be placed on Ω_M, $\Omega_{\rm DE}$, w_o, and w_1, assuming $w(z) = w_0 + w_1 z$ (see Figures 2-4).

Precursor observations are needed to determine $E^{\rm obs}_{\rm peak}$ S_E, $t_{\rm jet}$, and z for a much larger sample of GRBs, and to use this much larger sample of bursts to confirm that (1) most GRBs satisfy the $E_{\rm peak} - E_{\rm iso} - t_{\rm jet}$ relation, (2) this relation extends down in $E_{\rm iso}$ and $E_{\rm peak}$ to XRFs, (3) the systematic errors in this relation are small, and (4) X-ray afterglow observations can accurately determine $t_{\rm jet}$ for most bursts, including XRFs, for which $t_{\rm jet}$ can be as large as ~ 20 days.

Confirming each of these four items will require (1) the prompt localization of many more GRBs and XRFs; (2) the measurement of their observed peak energy $E^{\rm obs}_{\rm peak}$, and fluence S_E; (3) the determination of their jet break time $t_{\rm jet}$; and (4) the measurement of their redshift z. *HETE-2* and *Swift*, working together, can do (1) very well, enabling ground-based telescopes to do (4). *HETE-2* is ideally suited to do (2), whereas the *Swift* BAT (which has a relatively narrow energy band: 15 keV $< E <$ 150 keV) cannot. *Swift* XRT is ideally suited to do (3), whereas *HETE-2* cannot. However, a scientific partnership between *HETE-2* and *Swift* can obtain the necessary precursor observations.

This scientific partnership works in two ways: (1) a few bursts will be observed by both satellites, since *HETE-2* points anti-sun and *Swift* is biasing its spacecraft pointing direction toward the anti-sun direction as much as it can; and (2) *Swift* can slew to the 20-25 bursts per year

that *HETE-2* localizes and for which it measures $E_{\rm peak}^{\rm obs}$ and S_E. The former has already happened for GRBs 050215b (Sakamoto et al. 2005b) and 050401 (Atteia 2005; Barbier et al. 2005); the latter has already happened for GRBs 050209 (Kawai et al. 2005) and 050408 (Sakamoto et al. 2005c; Wells et al. 2005).

Of the 20-25 bursts per year that *HETE-2* localizes, ≈ 7 are GRBs, ≈ 7 are XRRs, and ≈ 9 are XRFs. This implies that, in three years of partnership with *Swift*, *HETE-2* will localize and determine $E_{\rm peak}^{\rm obs}$ and $E_{\rm iso}$ for ≈ 21 GRBs and XRRs, and ≈ 27 XRFs, giving a total of ~ 70 bursts of which it can reasonably be expected that ≈ 55 will have all four quantities measured. A few additional bursts localized by *Swift* will have their $E_{\rm peak}^{\rm obs}$ and S_E measured by *Konus-Wind*. Thus precursor observations can provide ≈ 60 additional "Gold" bursts – nearly doubling the size of the current sample of bursts with known redshifts, quintupling the size of the current sample of "Gold" bursts, and increasing the number of XRFs with known redshifts from two to 15-20 [XRFs 020903 (Soderberg et al. 2004) and 040701 (Kelson et al. 2003) are the only XRFs with accurately known redshifts; redshift constraints exist for two others: XRFs 020427 (Amati et al. 2004) and 030723 (Fynbo et al. 2004)]. The full sample of ≈ 70 "Gold" bursts will enable a much more stringent test of the degree to which GRBs obey the $E_{\rm peak} - E_{\rm iso} - t_{\rm jet}$ relation, particularly XRFs. In particular, confirmation that XRFs obey the $E_{\rm peak} - E_{\rm iso} - t_{\rm jet}$ relation would make it possible to use them to calibrate the relation (see below), and to increase the power of the constraints on w_0 and w_a (also see below).

2. Error Budget

Statistical Errors: The primary sources of statistical errors are the uncertainties with which the spectral parameters $E_{\rm peak}^{\rm obs}$, S_E, and the jet break time $t_{\rm jet}$, can be determined. In addition, there are sample variances in the $E_{\rm peak} - E_{\rm iso}$ and $E_{\rm peak} - E_\gamma$ relations of sizes 0.2 and 0.1 dex, respectively. Here we assume Gaussian distributions perpendicular to both the best-fit $E_{\rm peak} - E_{\rm iso}$ and the best-fit $E_{\rm peak} - E_\gamma$ relations with widths $\sigma = 0.4$ and $\sigma = 0.15$, respectively. These widths accurately characterize the current statistical plus sample variances in these distributions. We assume 20% errors in both $E_{\rm peak}$ and $t_{\rm jet}$, and 10% errors in the fluence S_E. The accuracies with which the parameters (intercepts C, slopes s, and intrinsic widths σ) of the $E_{\rm peak}$-$E_{\rm iso}$ and $E_{\rm peak}$-E_γ relations can be determined scale as $1/\sqrt{N_{\rm GRB}}$, where $N_{\rm GRB}$ is the number of bursts in the sample used. The uncertainties in the determination of Ω_M, $\Omega_{\rm DE}$, w_0, and w_a, therefore scale similarly.

The scientific partnership between *HETE-2* and *Swift* discussed in the previous section can produce significantly better determinations of the spectral parameters $E_{\rm peak}$, $E_{\rm iso}$, and E_γ of the burst, and the jet break time $t_{\rm jet}$, especially for the important XRFs. The mission concept that we propose would produce much better determinations of these quantities. Nevertheless, here we assume the previous accuracies with which these quantities can be determined (i.e., 10% errors in S_E and 20% errors in $E_{\rm peak}^{\rm obs}$ and $t_{\rm jet}$). In this sense, the results that we report in this white paper are very conservative.

Systematic Errors: The use of GRBs to constrain the properties of dark energy is in its infancy compared with many of the other approaches that are being used and proposed. We acknowledge that in this situation, the risk that systematic errors may prevent this approach from reaching the accuracy necessary to tightly con-

strain w_0 and especially, to remove the degeneracy between w_0 and w_a that exists if CMB priors are used (as we do) may be greater than in some other methods. However, there are reasons to believe that GRBs may suffer less from systematic errors than some other approaches.

Friedman & Bloom (2005) have discussed a number of possible sources of systematic errors in using GRBs as standard candles. Ghirlanda et al. (2005) and Firmani et al. (2005) have addressed many of these. In addition, very recent work by Liang & Zhang (2005) has shown that the $E_{\rm peak} - E_{\rm iso} - E_\gamma$ relation can be put on an entirely empirical footing by writing it in terms of $E_{\rm peak} - E_{\rm iso} - t_{\rm jet}$. This approach has the advantage of making the relation explicitly model-independent, and eliminates the need to marginalize over the density n of the circumburst medium.

Perhaps the most worrying kind of systematic error for relative standard candles is one that would mimic the effect of dark energy; e.g., calibration errors that would produce a bump in the inferred intrinsic brightness over the redshift range $0.6 \lesssim z \lesssim 1$ (i.e., $\Delta z/z \approx 40\%$, corresponding to energy or wavelength ranges $\Delta E/E \approx \Delta\lambda/\lambda \approx 40\%$). GRBs may be less prone to this particular kind of systematic error than other standard candles for several reasons. First, the determinations of z and $t_{\rm jet}$ are not subject to this kind of systematic error. Second, the spectra of GRBs are smoothly broken power laws that span a broad energy range and that have a peak energy in νF_ν that is broad. Third, while the detector response matrices (DRMs) of gamma-ray detectors (e.g, NaI) have an absorption feature at $E \approx 37$ kev, the DRMs are not diagonal: because of Compton scattering and other effects, a beam of mono-energetic photons produces counts in a range of energy loss bins, which smooths the detector response as a function of energy. These properties of GRB spectra and detectors lessens the probability that systematic errors of the kind that would mimic the effect of dark energy can occur.

Self-Calibration: The $E_{\rm peak} - E_{\rm iso} - t_{\rm jet}$ relation is cosmology dependent because $E_{\rm iso}$ depends on cosmology (Ghirlanda et al. 2004b). However, the fact that the 15 bursts in the current "Gold" sample of GRBs span the broad redshift range $z = 0.17$ - 3.2 is evidence that the relation does not evolve with redshift; i.e., it is independent of z. Assuming that the $E_{\rm peak} - E_{\rm iso} - t_{\rm jet}$ relation is independent of z, a self-calibration approach can be used to eliminate the dependence of its slope on cosmology. In this approach, either a sample of XRFs at low redshifts or a sample of GRBs in a narrow redshift range at high redshifts can be used to determine the relation, independent of cosmology. Figure 5 illustrates the latter approach. It shows that, using this method, the slope of the relation can be calibrated to $< 1\%$ accuracy, independent of cosmology. Comparisons of the parameters that define the relation for different redshift intervals, and for bursts at low redshift, can be used to check that the slope of the relation is indeed independent of cosmology. Figure 6 illustrates the much smaller sizes of the confidence regions that result when the slope of the $E_{\rm peak} - E_\gamma$ relation is known, independent of cosmology.

Lastly, the mission concept that we are proposing would provide a data base of > 800 bursts with well-determined spectral parameters, jet break times, and redshifts that will be an order of magnitude larger than the sample of such bursts that will be produced by the scientific partnership between *HETE-2* and *Swift* . This large sample of "Gold" bursts will enable a search for the best empirical relationship among the spec-

tral parameters, the jet break time of the afterglow, and the redshift thus tightening the constraints on the properties of dark energy. It will also provide an unprecedented data base for gaining a new understanding of GRB jets – and therefore minimizing – possible sources of systematic error.

3. Constraints on Nature of Dark Energy

Scaling from the burst rate seen by BATSE, *Beppo*SAX , and *HETE-2* , the mission concept we are proposing would localize and obtain the spectra for $\approx$ 800 GRBs per year, or 1600 during a 2-year mission, of which 200 per year, or 400 during a 2-year mission, would be XRFs. The percentage of *HETE-2* bursts for which redshifts have been obtained during the past three years is $\sim$ 30%; however, most of these bursts had $7' - 10'$ WXM localizations, requiring relatively wide-field optical cameras to identify the optical afterglow, a prerequisite to determining the redshift of the burst from absorption lines in the afterglow spectrum. In contrast, the mission concept that we are proposing would obtain and disseminate arcsecond burst localizations in real time. We therefore estimate that redshifts will be obtained for 50% of the bursts that the mission localizes, a percentage that we regard as quite conservative. This gives 400 bursts per year, or 800 bursts in a 2-year mission, with well-measured values of $E^{\rm obs}_{\rm peak}$, S_E, $t_{\rm jet}$, and z.

We compute the constraints that GRBs can place on the properties of dark energy as follows. First, we generate a catalog of 800 GRBs with spectral properties matching the distributions of the spectral properties of GRBs seen by *Beppo*SAX and *HETE-2* and a redshift distribution matching the inferred star formation rate as a function of redshift (see Figure 7). We parameterize the dark energy equation of state $w(z)$ as a function of redshift by the phenomenological expression (Linder 2003) $w(z) = w_0 + (1-a)w_a$, where $a = 1/(1+z)$ is the scale factor of the universe. In constructing the catalog of simulated bursts, we assume $\Omega_M = 0.30$ and $\Omega_{\rm DE} = 0.7$, $w_0 = -1$, and $w_a = 0$ (i.e., a spatially flat, vanilla ΛCDM cosmology).

We determine the best-fit cosmology and 68%, 90%, and 99% confidence regions by comparing the luminosity distance $d_L(z)$ for various cosmologies with the distribution of $d_L^{\rm GRB}$ values for the 800 GRBs in our simulated burst sample, using χ^2 as the statistic. In doing so, we employ two CMB priors: $\Omega_M + \Omega_{\rm DE} = 1$ (a flat universe) and $\Omega_M h^2 = 0.14$. Because Planck is expected to determine the value of the latter to $< 1\%$, and to simplify the computations, we assume that both priors have zero uncertainty. Given these priors, $d_L(z)$ is a function only of H_0, w_0, and w_a. We consider three cases:

1. We first assume that $w_0 = -1$ and $w_a = 0$. The only free parameter is then H_0. Figure 8 shows the resulting posterior probability distributions for Ω_M and $\Omega_{\rm DE}$.

2. We assume that $w_a = 0$. The free parameters are then H_0 and w_0. Figure 9 (top panel) shows the resulting 68%, 90%, and 99% confidence regions in the (Ω_M, w_0)-plane. Figure 9 (bottom panel) is the same, except that we also employ the prior $H_0 = 68 \pm 8$ km s^{-1} Mpc^{-1} after the HST key project (Freedman et al. 2001), but adopting a best-fit value for H_0 that is consistent with the values of Ω_M and $\Omega_{\rm DE}$ that we used in constructing our catalog of simulated bursts.

3. We make no assumptions about w_0 and w_a. We again employ the prior on H_0 from the

HST key project, but to simplify the computations we assume that it has zero uncertainty (this is a good approximation, since the constraints derived on w_0 and w_a are much larger than this.) The free parameters are then w_0 and w_a. Figure 10 shows the resulting 68%, 90%, and 99% confidence regions in the (w_0,w_a)-plane.

Table 1 gives the 1-σ uncertainties in the dark energy parameters for each of the above cases, marginalized over the other parameters. The assumed values of the parameters lie within the 68% confidence regions but not at their centers (unlike Fisher matrices) because we use a simulated catalog of GRBs.

GRBs, like Type Ia SNe, are "relative" standard candles, in the sense that their intrinsic luminosities are not determined; instead, their relative brightnesses are compared at different redshifts. Many GRBs occur and can be observed at high redshift. Using CMB priors then provides an absolute calibration (Hu 2005). In this case, one is measuring $\Delta D/D$ and the most severe constraint on whether $w_0 = -1$ comes from GRBs observed at $z \lesssim 0.3$. This is opposite to the case for Type Ia SNe, since many Type Ia SNe occur at $z \lesssim 0.3$; then $\Delta H_0 D/H_0 D \rightarrow \Delta H_0/H_0$, and the most severe constraint on whether $w_0 = -1$ comes from Type Ia SNe observed at redshifts $z > 1$ (see Figure 11).

Therefore, in order to exploit the power that comes from using CMB priors, a sufficient number of bursts must be observed at very low redshifts. If the precursor observations described above confirm that XRFs satisfy the $E_{\rm peak} - E_{\rm iso} - t_{\rm jet}$ relation, XRFs can provide the population of relative standard candles at $z \sim 0$ that is needed: XRFs have redshifts $z \lesssim 0.5$ and by adjusting the design of the proposed mission concept, as many as 200-300 XRFs could be obtained at very low redshifts. Alternatively, the complementary redshift ranges of Type Ia SNe ($0 \lesssim z \lesssim 1.7$) and classical GRBs ($0.5 \lesssim z \lesssim 10$) could be exploited to provide a combined population of relative standard candles that spans the entire redshift range $0 \lesssim z \lesssim 10$, which could provide more severe constraints on the properties of dark energy than could either population alone.

4. Proposed Mission Concept

The mission concept (see Appendix A) is optimized to use GRBs as "standard candles" to determine the properties of Dark Energy and probe the early universe rather than increasing our understanding of GRBs and their precursors. In this sense, it is very different than previous GRB missions, including *Beppo*SAX, *HETE-2*, and *Swift*, although it will provide a great deal of information about the prompt and afterglow emission of a large number of bursts. The mission concept that we describe also builds on the "lessons learned" from previous GRB missions, including *Beppo*SAX, *HETE-2* , and *Swift*. In particular, it exploits the very recent discoveries that tight relations exist between $E_{\rm iso}$ and $E_{\rm peak}$, and between E_γ and $E_{\rm peak}$, and it combines the capabilities of all of these missions in a way that maximizes the scientific return of the mission for the purpose of determining the properties of dark energy.

As described more fully in Appendix A, the mission concept calls for three small spacecraft operating in near-proximity at the sun-earth L_2 point for two years with the following roles: (1) One Prompt Satellite (a "mini spacecraft," ~200 kg) to detect and fully characterize the prompt spectra of GRBs and XRFs over the 1-1000 keV band, as well as to establish their location to ~arcsecond accuracy. (2) Two Afterglow Satel-

lites ("micro spacecraft," ∼50 kg each) to measure the burst X-ray afterglow and to determine the time of the jet break. In addition, as described in Appendix B, the mission concept calls for: (3) A network of six fully-automated, two meter-class ground-based telescopes equipped with integral-field spectrometers (IFS) that will be dedicated to establishing redshifts for a large fraction (∼50%) of the localized GRBs and XRFs.

5. Other Issues

Risks and Strengths: This mission concept is based on a low-risk approach that relies on flight-proven technologies and the heritage of *HETE-2*. Redundancy is provided by a cluster of silicon X-ray CCD detectors and a set of NaI detectors on one satellite, and by two focusing X-ray telescope arrays, each on a separate satellite. The number of GRBs observed is large; the contribution of statistical errors to the uncertainties with which the dark energy parameters can be determined will be modest. The level at which systematic errors will dominate is not known, and represents a risk, but precursor observations can substantially reduce this risk. In addition, the properties of GRB spectra and gamma-ray detectors lessen the probability that systematic errors of the kind that would mimic the effect of dark energy can occur.

Technology Readiness: There are no complicated requirements on the satellites or the operations. The Prompt Satellite is of modest size; the X-ray CCD detectors are similar to those used in the Soft X-ray Camera (SXC) on *HETE-2* and the focal plane of *Chandra*, and the NaI detectors are nearly identical to those that have flown on numerous GRB missions over the past 30 years–most recently Fregate on *HETE-2*. The two X-Ray Afterglow Satellites are of very small size; the X-ray mirrors are of short focal length and are small in diameter. There X-ray CCD detectors are even smaller than those that were flown on *ASCA*. The required sensitivity for this mission concept is achieved primarily by greatly increasing the number of detector modules, so as to view a much larger solid angle ($\sim$ 10 times that of *HETE-2* and *Swift*) and by operating at L_2, which permits a much greater observing efficiency ($\sim$ 3 times that of *HETE-2*). The dedicated ground segment of the mission relies on purchasing six commercially-available two-meter class telescopes and equipping them with efficient, state-of-the-art integral field spectrometers. Thus, the mission concept relies on flight-proven technologies and established ground-based telescope systems, and is thus "ready to go."

Relationship to JDEM and LSST: The GRB Dark Energy mission is not a precursor to JDEM or LSST. Indeed, the significantly different parameter degeneracies of the constraints on the parameters that characterize Dark Energy that will come from the GRB Dark Energy mission make it complementary to JDEM and LSST, as well as to *Planck* and any X-ray survey of galaxy clusters.

Access to Facilities: All facilities that are needed for the baseline mission have been included as part of the mission. Ground-based optical follow-up observations using existing large-aperture ($>$ 6 meter) telescopes to determine the redshifts of some fainter bursts (e.g., some XRFs) would increase the number of bursts beyond that assumed in this white paper.

Timeline: The GRB dark energy mission discussed in this white paper is not currently funded. The baseline mission fits within the resources (time, mass, volume, and cost) of a NASA Medium Explorer mission. It could therefore be proposed for next Midex AO and flown 4 years later (e.g., in $\sim$ 2011).

REFERENCES

Amati, L., et al. 2002, A&A, 390, 81

Amati, L., et al. 2004, A&A, 426, 415

Atteia, J.-L. 2005, private communication

Barbier, L., et al. 2005, GCN Circular No. 3162

Bloom, J. S., Frail, D. A., & Kulkarni, S. R. 2003, ApJ, 594, 674

Firmani, C., Ghisellini, G., Ghirlanda, G., & Avila-Reese, V. 2005, MNRAS, 360, L1

Frail, D. A., et al. 2001, ApJ, 562, L55

Freedman, W. L., et al. 2001, ApJ, 553, 47

Friedman, A. S. & Bloom, J. S. 2005, ApJ, 627, 1

Fynbo, J. P. U., et al. 2004, ApJ, 609, 962

Ghirlanda, G., Ghisellini, G., & Lazzati, D. 2004a, ApJ, 616, 331

Ghirlanda, G., Ghisellini, G., Lazzati, D., & Firmani, C. 2004b, ApJ, 613, L13

Ghirlanda G., Ghisellini, G., Lazzati, D. & Firmani, C. 2005, in Proceedings of the Fourth Rome Workshop on GRBs in the Afterglow Era, Il Nuovo Cimento, in press (astro-ph/0504184)

Hamuy, M. et al. 1996, AJ, 112, 2398

Hu, W. 2005, ApJ, in press (astro-ph/0407158)

Kawai, N., et al. 2005, GCN Circular No. 3013

Kelson, D. D., et al. 2003, GCN Circular No. 2627

Lamb, D. Q., & Reichart, D. E. 2000, ApJ, 536, 1

Lamb, D. Q., et al. 2004, New Astronomy, 48, 423

Liang, E., & Zhang, B. 2005, ApJ, submitted (astro-ph/0504404)

Linder, E. V. 2003, PRL, 90, 091301

Perlmutter, S., et al. 1999, ApJ, 517, 565

Riess, A. G., et al. 2004, ApJ, 607, 665 (R04)

Rowan-Robinson, M. 2001, APJ, 549, 745

Sakamoto, T., et al. 2004, ApJ, 602, 875

Sakamoto, T., et al. 2005a, ApJ, in press (astro-ph/0409128)

Sakamoto, T., et al. 2005b, ApJ, to be submitted

Sakamoto, T., et al. 2005c, GCN Circular No. 3189

Soderberg, A. M., et al. 2004, ApJ, 606, 994

Spergel, D. N. et al. 2003, APJS, 148, 175

Wells, A. A., et al. 2005, GCN Circular No. 3191

Table 1. Dark energy parameter constraints from 800 GRBs.[a]

Priors[a]	$\sigma(\Omega_{\rm DE})^b$	$\sigma(w_0)^b$	$\sigma(w_{\rm a})^b$
$w_0 = -1$, $w_{\rm a} = 0$	-0.0076, $+0.0142$	—	—
$h = 0.68 \pm 0.08$, $w_{\rm a} = 0$	± 0.070	± 0.061	—
$\Omega_M \equiv 0.3$	—	-0.2, $+0.32$	-1.12, $+0.63$

[a]All results assume CMB priors (i.e., $\Omega_M + \Omega_{\rm DE} = 1$ and $\Omega_M h^2 = 0.14$), in addition to the priors listed.

[b]All confidence regions are 68.3% CL.

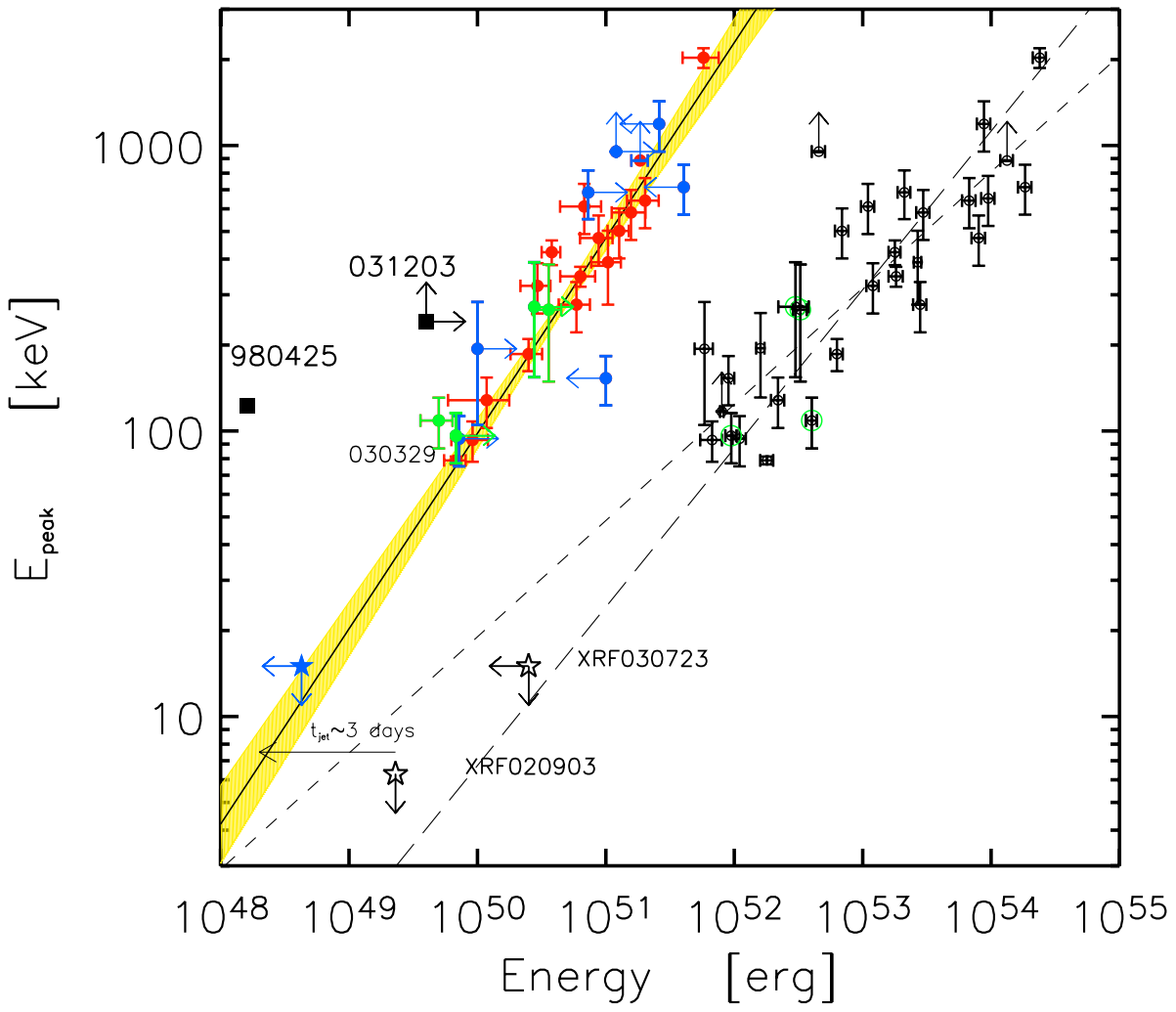

Fig. 1.— The rest frame $E_{\rm peak}$–$E_{\rm iso}/E_\gamma$ plane. Black open symbols represent the isotropic equivalent energy. Red filled symbols are the 15 GRBs for which a jet break was measured in their afterglow light curves. Blue symbols are upper/lower limits for E_γ. The four new GRBs are represented as open green circles for $E_{\rm iso}$ and filled green symbols for E_γ. Also shown are two outliers (black squares) for either the Amati and the Ghirlanda correlation (filled squares). Stars are the two XRF with known redshift. The Amati correlation is also reported either fitting with the errors on both coordinates (long dashed line) and with the least square method (dashed line). The best fit Ghirlanda correlation (solid black line), giving a reduced $\chi^2 = 1.33$ and a slope ~ 0.7, is also shown with its uncertainty region (shaded area). (Figure from (Ghirlanda et al. 2005)).

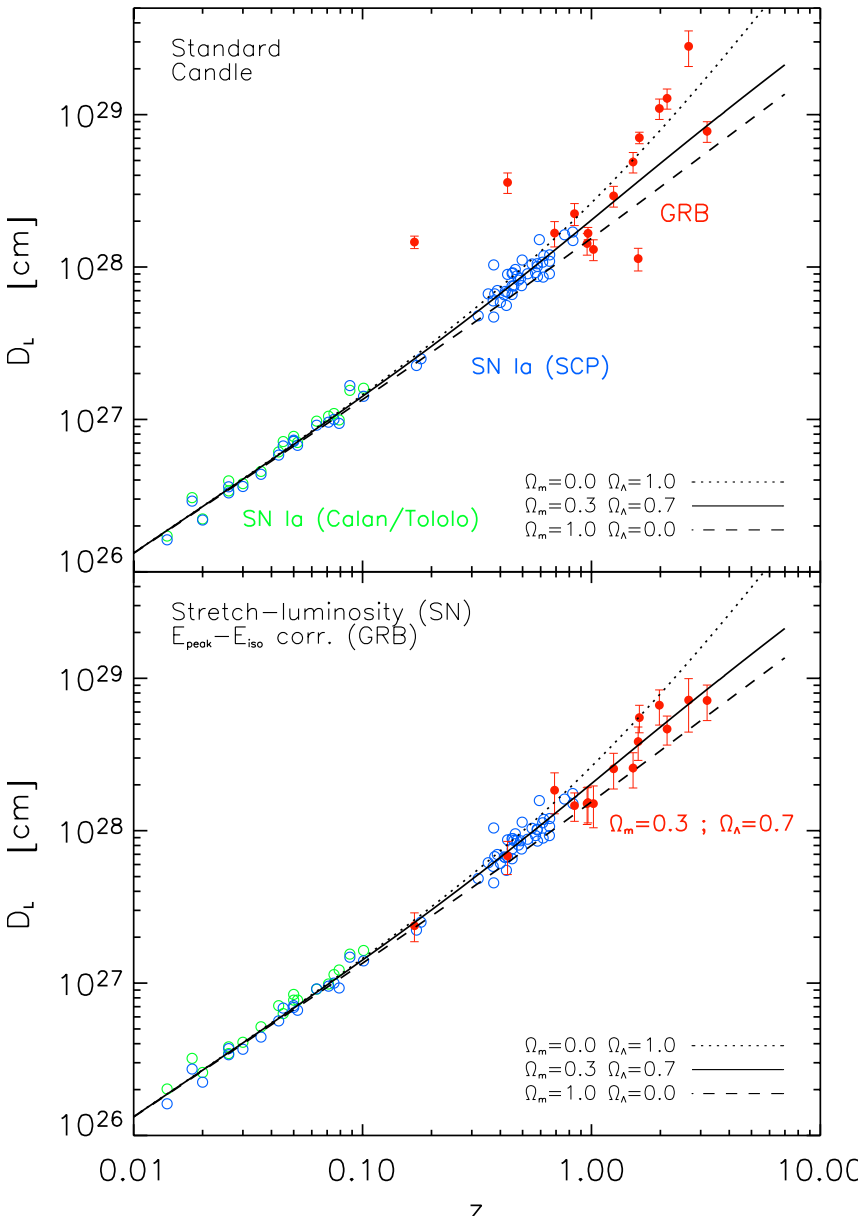

Fig. 2.— Classical Hubble diagram in the form of luminosity–distance $D_{\rm L}$ vs. redshift z for Supernova Ia (open green circles: Calàn/Tololo sample (Hamuy et al. 1996); open blue circles: Perlmutter et al. 1999) and GRBs (filled red circles: the 15 bursts in Ghirlanda et al. 2004b). In the top panel the SN Ia and GRBs are treated as standard candles (no corrections applied); for GRBs $E_\gamma = 10^{51}$ erg is assumed. In the bottom panel, we have applied the stretching–luminosity and the E_γ–$E_{\rm peak}$ relations to SN Ia and GRBs, respectively, as explained in the text. Note that, for GRBs, the applied correction depends upon the assumed cosmology: here we assume the standard $\Omega_M = 0.3$, $\Omega_{\rm DE} = 0.7$ cosmology. Both panels also show different $D_{\rm L}(z)$ curves, as labelled. ¿From Ghirlanda et al. (2004b).

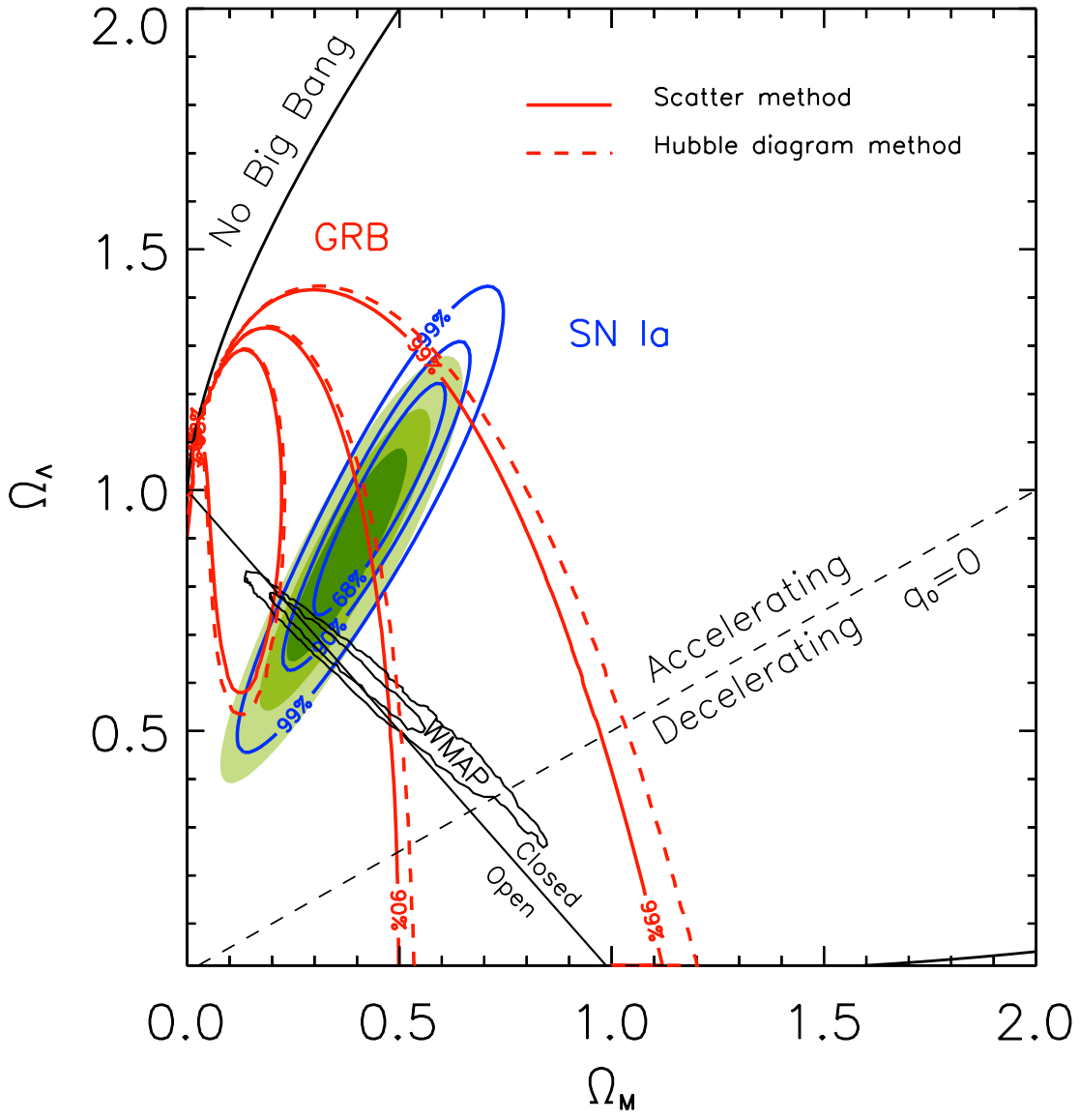

Fig. 3.— Constraints in the $\Omega_M - \Omega_{\rm DE}$ ($\Omega_{\rm DE} = \Omega_\Lambda$) plane derived for our GRB sample (15 objects, red contours); the "Gold" Supernova Ia sample of R04) (156 objects, blue contours, derived assuming a fixed value of $H_0 = 65$ km s^{-1} Mpc^{-1}, making the contours slightly different from Fig. 8 of R04). The WMAP satellite constraints (black contours, Spergel et al. 2003) are also shown. The three colored ellipsoids are the confidence regions (dark green: 68%; green: 90%; light green: 99%) for the combined fit of SN Ia and our GRB sample. For GRBs only, the minimum $\chi^2_{red} = 1.04$, is at $\Omega_M = 0.07$, $\Omega_{\rm DE} = 1.2$. From Ghirlanda et al. (2004b).

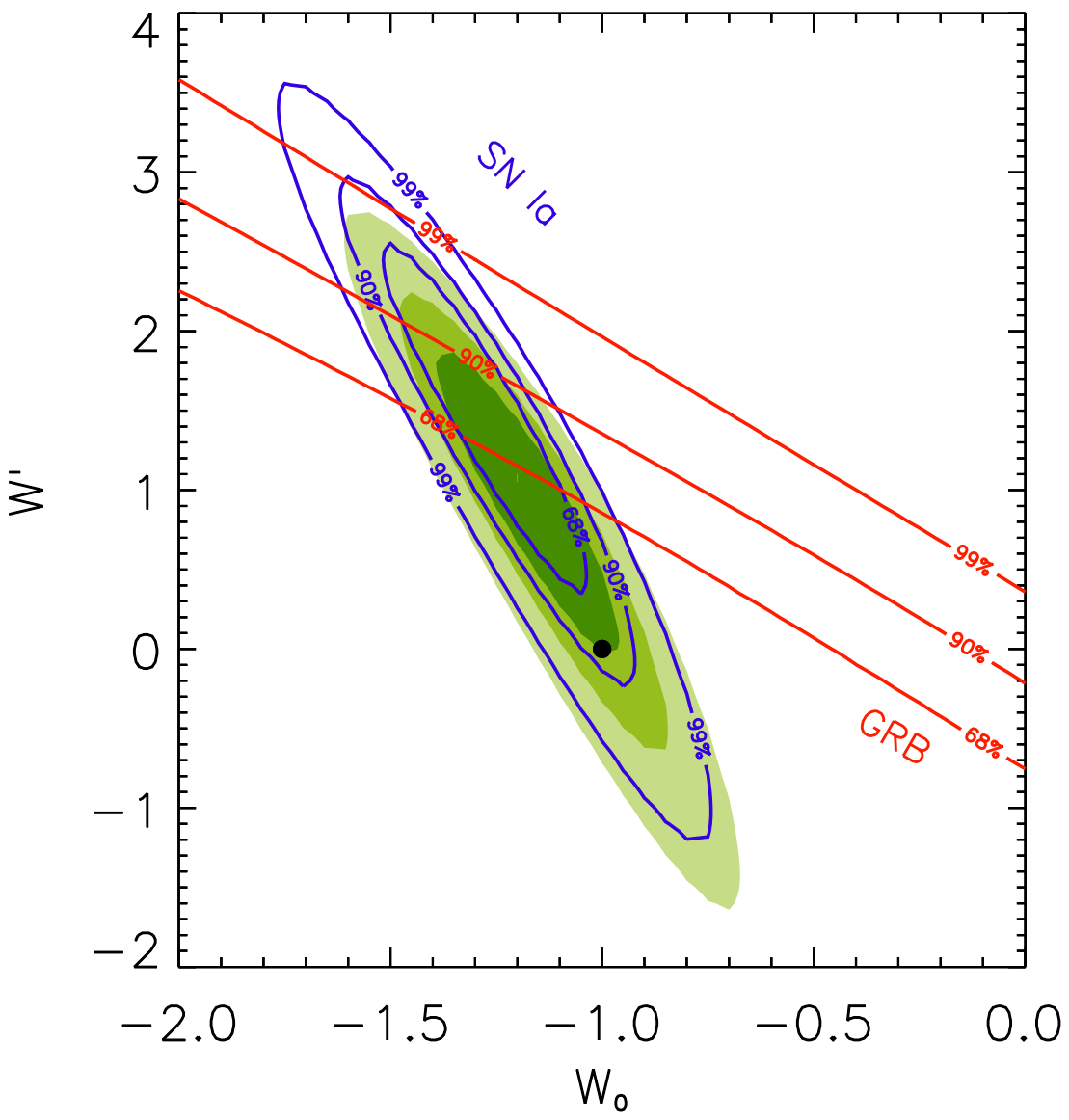

Fig. 4.— Constraints on the w_0, w' parameters entering the equation of state $p = (w_0 + w'z)\rho c^2$, where ρ is the dark energy density. $w_0 = -1$ and $w' = 0$ correspond to the cosmological constant $\Omega_{\rm DE}$. We assume a flat geometry and $\Omega_M = 0.27$ (see also R04). Blue contours: constraints from type Ia SN (R04). Red contours: constraints from our GRBs, Colored regions: combined constraints (dark green, green and light green for the 68%, 90% and 99% confidence levels, respectively). From Ghirlanda et al. (2004b).

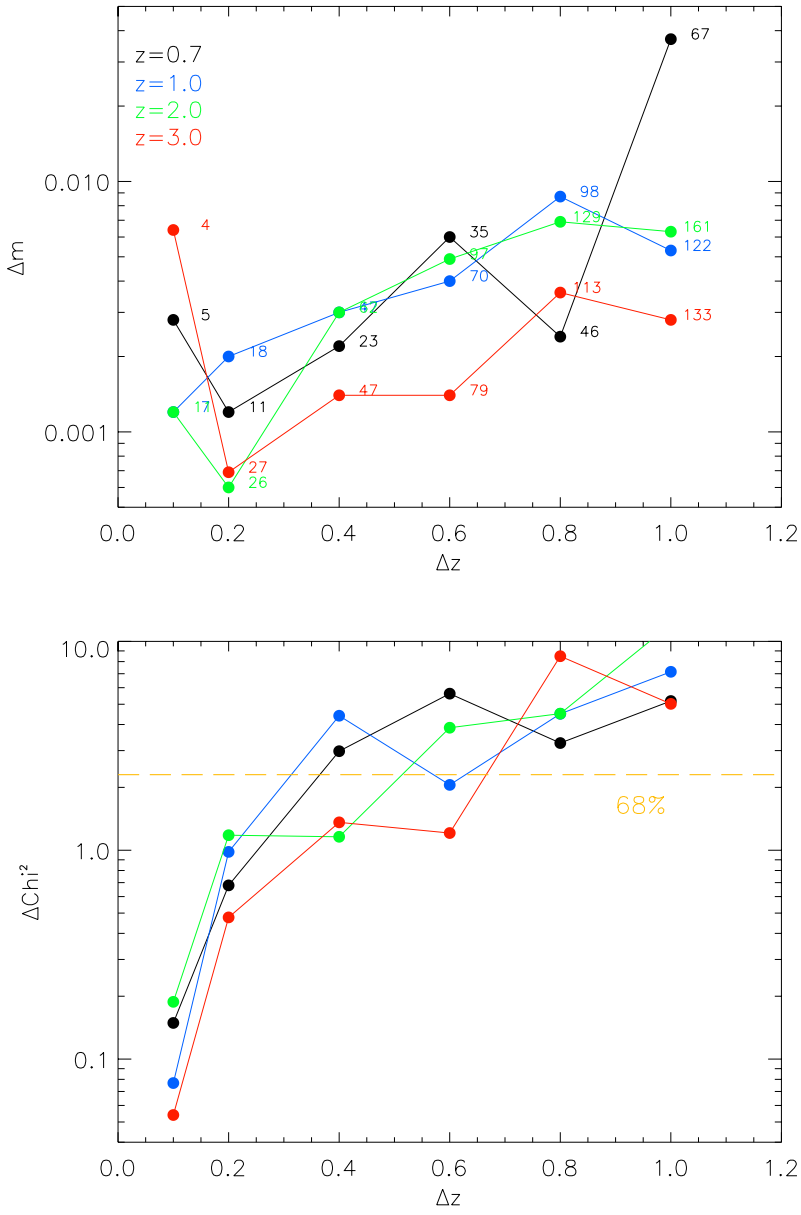

Fig. 5.— Illustration of the self–calibration method for the $E_{\rm peak} - E_{\rm iso}$ relation. For different redshift "slices" Δz, centered on redshifts $z = 0.7$, 1.0, 2.0, and 3.0, the following quantities are shown: Top panel: Maximum variation δm in the slope m of the $E_{\rm peak} - E_\gamma$ correlation, obtained from surveying large ranges in the cosmological parameters Ω_M and $\Omega_{\rm DE}$. The numbers next to each point are the number of bursts in that particular redshift slice. Bottom panel: Maximum variation in χ^2 obtained from surveying large ranges in the cosmological parameters Ω_M and $\Omega_{\rm DE}$. Also shown is the 68% confidence level. A value of $\Delta\chi^2$ below this level ensures that the $E_{\rm peak} - E_{\rm iso}$ relation found using that redshift range (i.e., that size of Δz) is cosmology independent.

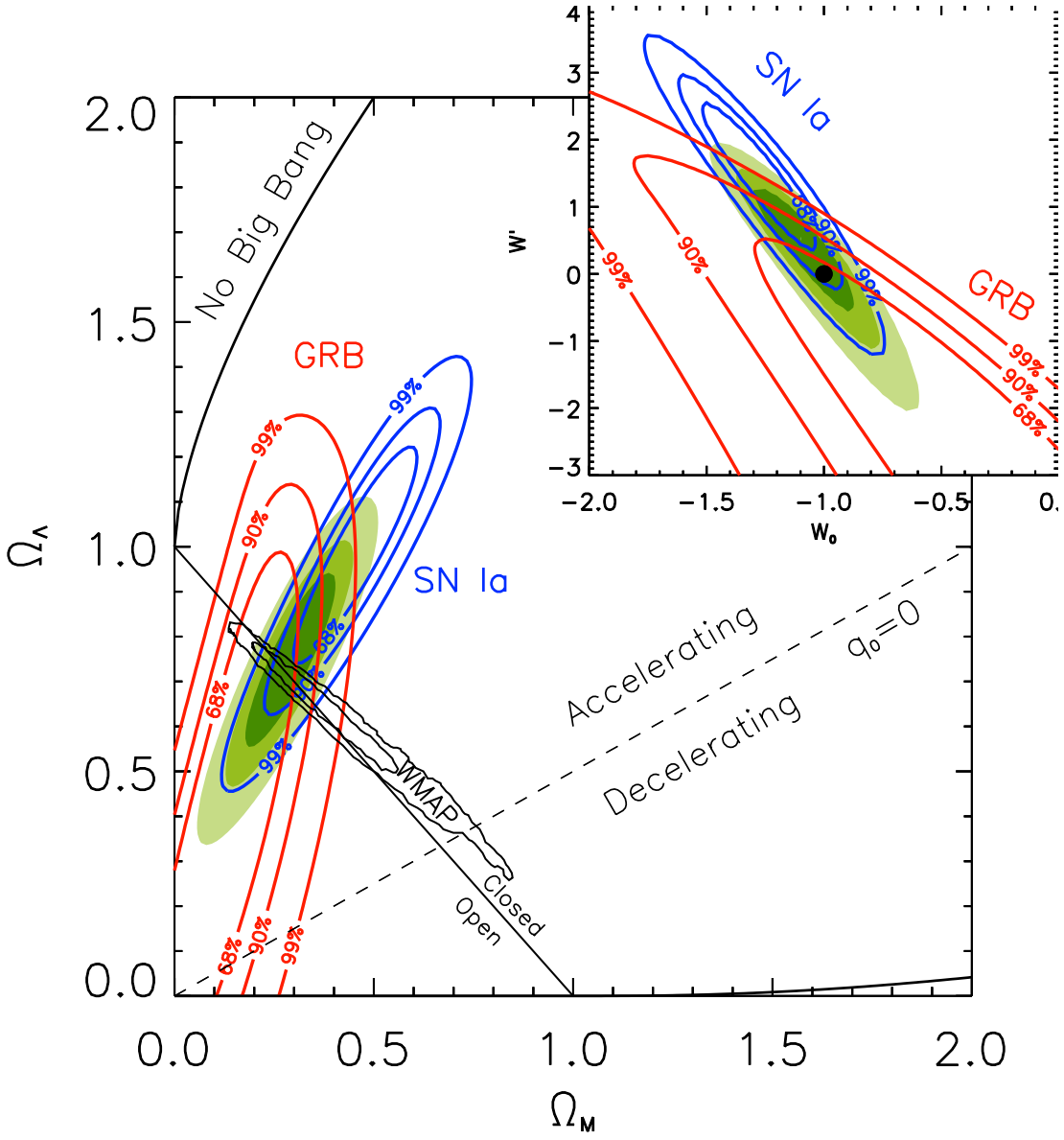

Fig. 6.— Example of how GRBs can contribute to the determination of the cosmological parameters once the $E_\gamma - E_{\rm peak}$ correlation can be determined in a cosmology-independent way [i.e., accumulating sufficient bursts at small redshifts or in a small redshift range (e.g. around $z = 2$)]. We show the contours in both the $(\Omega_M, \Omega_{\rm DE})$- plane ($\Omega_{\rm DE} = \Omega_\Lambda$ in main figure) and in the $w_0 - w'$ plane (insert, a flat cosmology with $\Omega_M = 0.27$ is assumed). Lines and colors are as in Fig. 2 and Fig. 3. (Figure from Ghirlanda et al. (2004b)).

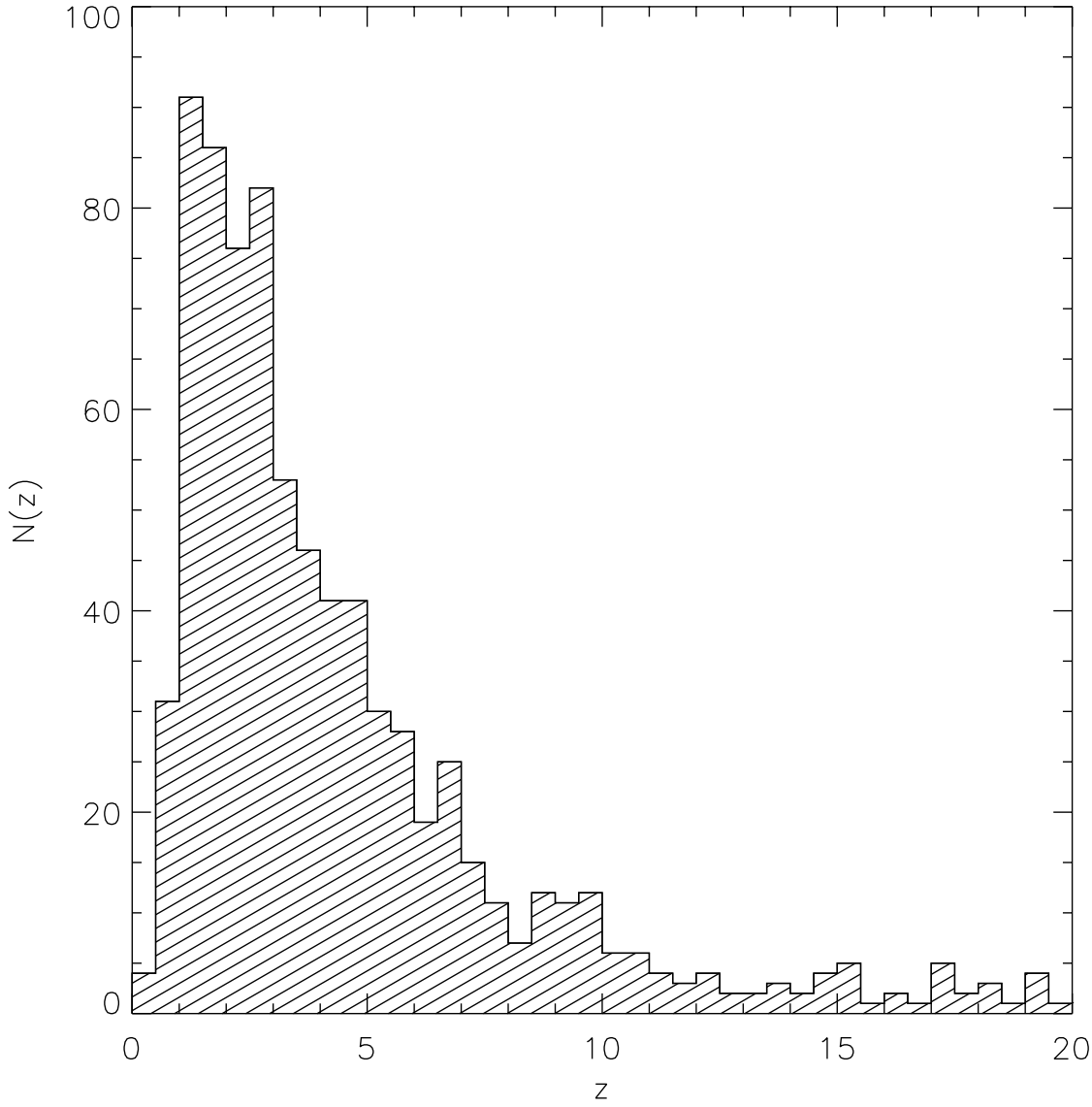

Fig. 7.— Distribution of GRBs as a function of redshift in our simulated catalog of 800 bursts. The distribution of GRBs is proportional to the phenomenological expression for the star formation rate (SFR) suggested by Rowan-Robinson (2001), adopting the parameter values $P = 1.2$ and $Q = 5.4$ (which provides a good fit to existing data on the SFR as a function of redshift). With this choice of the SFR and the nominal mission design, the catalog contains 35 GRBs at $z < 1$. However, XRFs have redshifts $z \lesssim 0.5$, and by adjusting the design of the proposed mission concept, the catalog could contain as many as 200-300 XRFs at very low redshifts.

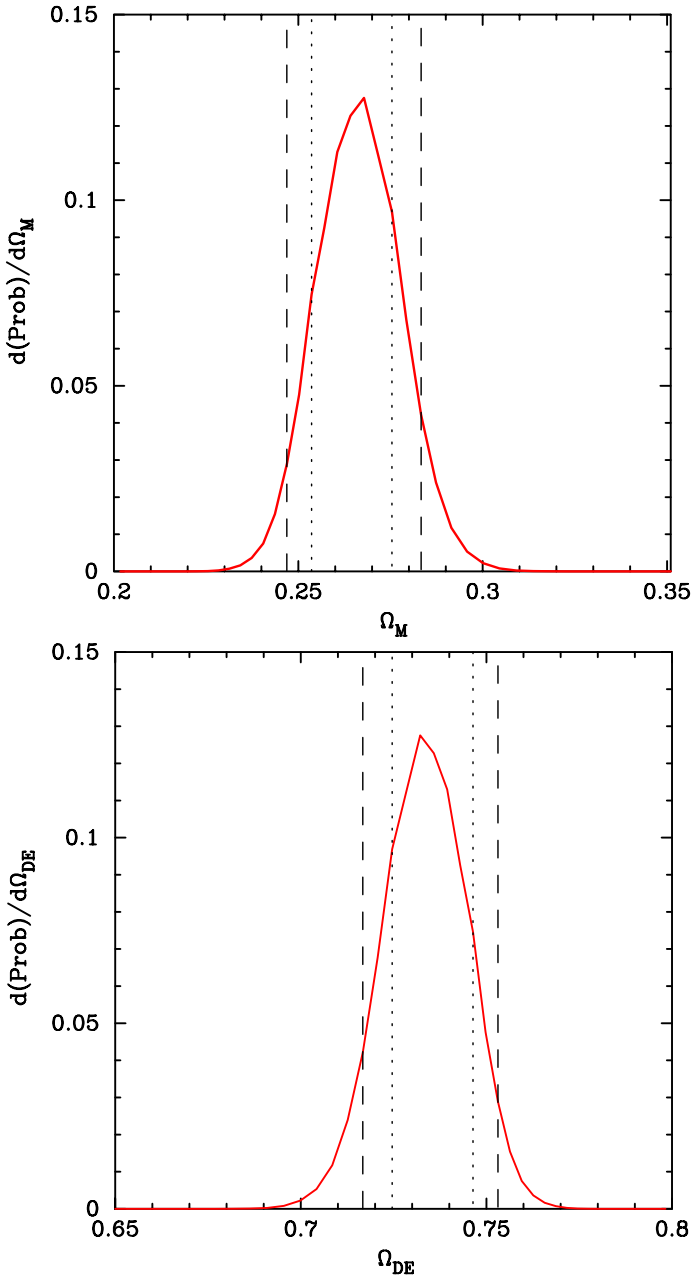

Fig. 8.— Constraints on Ω_M and $\Omega_{\rm DE}$ for 800 GRBs, using CMB priors (the only free parameter is then H_0). Top panel: posterior probability distribution for Ω_M. Bottom panel: posterior probability distribution for $\Omega_{\rm DE}$. The dotted lines show the 68% credible regions; the dashed lines show the 90% credible regions.

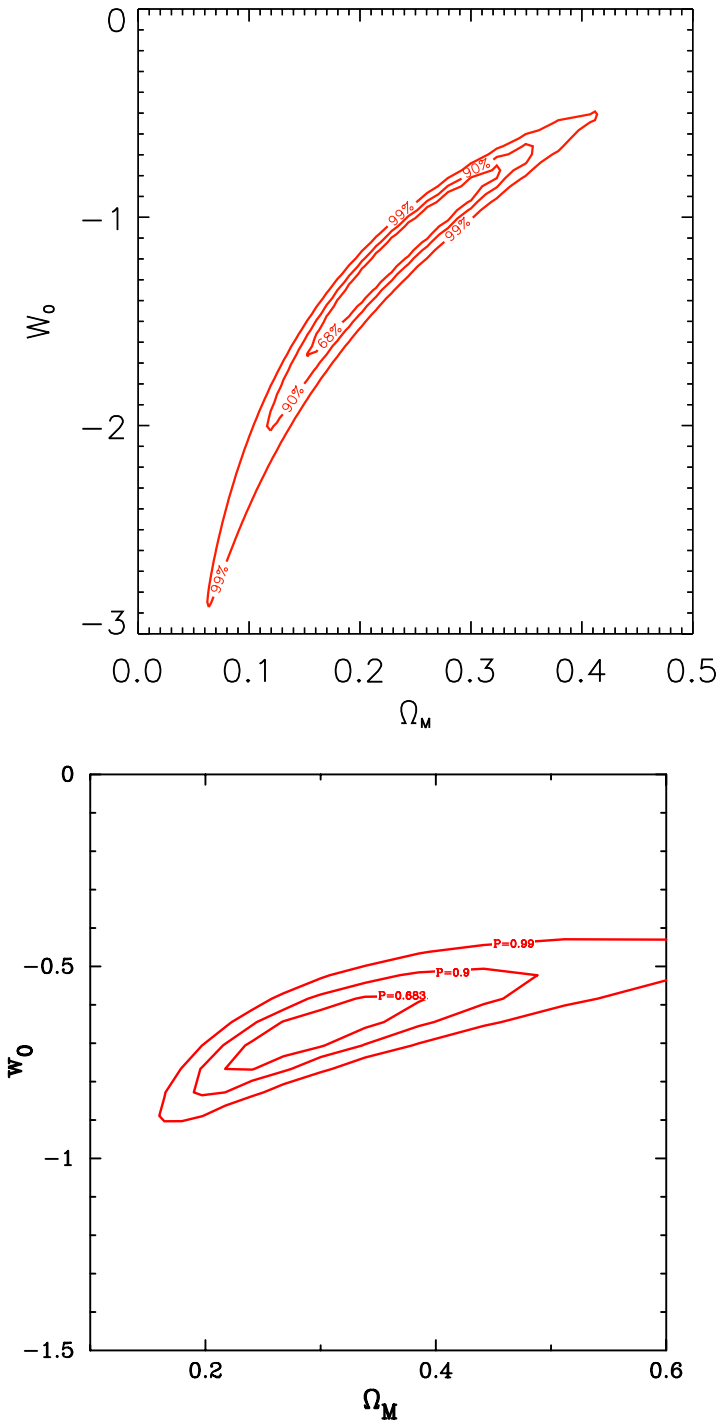

Fig. 9.— Top panel: Ω_M versus w_0 for 800 GRBs and using CMB priors. Bottom panel: the same, except that we also use the prior $H_0 = 68 \pm 8$ km s^{-1} Mpc^{-1} after the HST key project (Freedman et al. 2001).

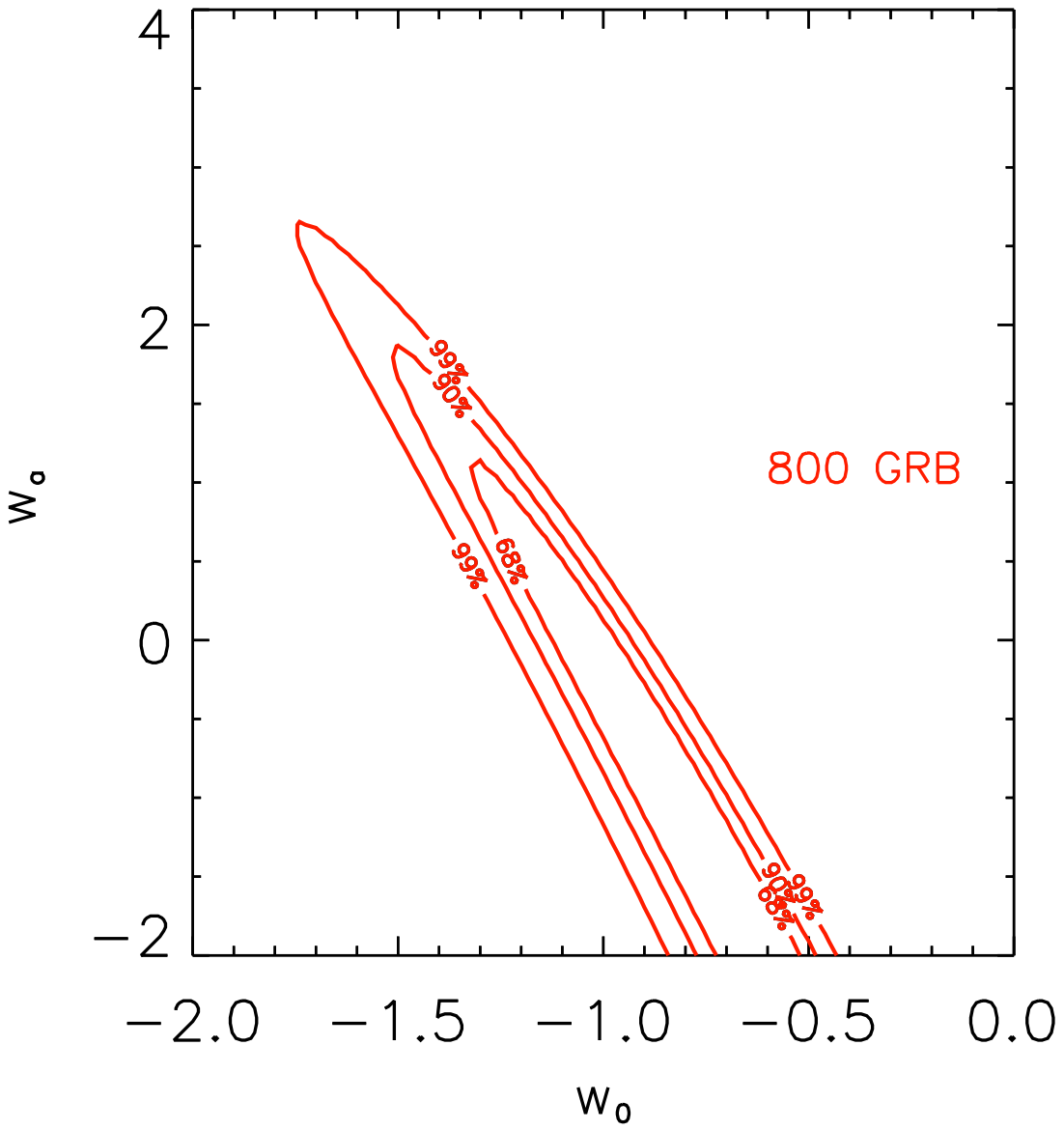

Fig. 10.— Constraints on w_0 and w_a for 800 GRBs, using CMB priors and the prior $H_0 = 68$ km s^{-1} Mpc^{-1} after the HST key project (Freedman et al. 2001). The last prior is a good approximation, since the constraints derived on w_0 and w_a are much larger than this. However, using the correct prior, $H_0 = 68 \pm 8$ km s^{-1} Mpc^{-1} [after the HST key project (Freedman et al. 2001)], would widen the contours in the direction perpendicular to their long axes.

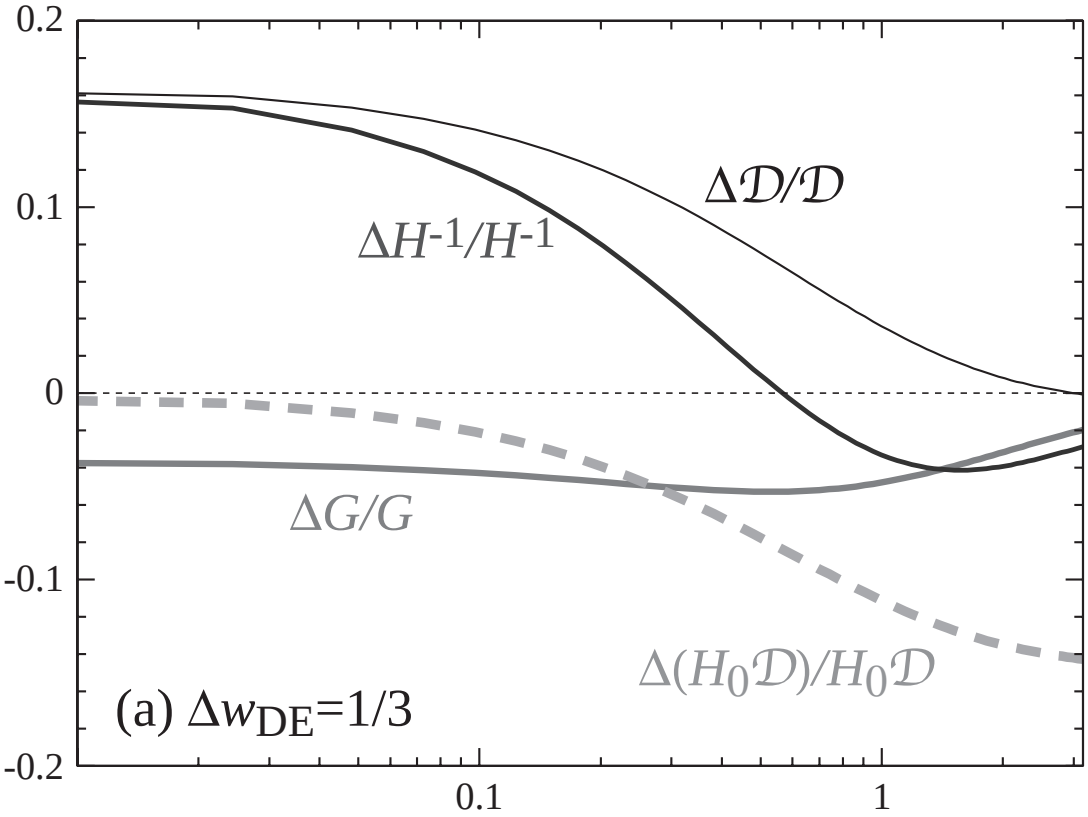

Fig. 11.— Sensitivity of determination of w_0, (assuming $w_a = 0$) as a function of redshift for various quantities. Both GRBs and Type Ia SNe are "relative standard candles," in the sense that their intrinsic luminosities are not determined; instead, their relative brightnesses are compared at different redshifts. Many GRBs occur and can be observed at high redshift. Using CMB priors then provides an absolute calibration (Hu 2005). In this case, one is measuring $\Delta D/D$ and the strongest constraints on whether $w_0 = -1$ come from GRBs observed at $z \lesssim 0.3$. This is opposite to the case for Type Ia SNe, since many Type Ia SNe have been observed at $z \lesssim 0.3$; then $\Delta H_0 D/H_0 D \to \Delta H_0/H_0$, and the strongest constraints on whether $w_0 = -1$ come from Type Ia SNe observed at redshifts $z > 1$. From Hu (2005).

Appendices: Instrumentation Concept for GRB Dark Energy Investigation

Introduction

As outlined in the text, for each of the 800 GRBs in the sample, we need to measure the spectral peak, $E_{\rm peak}$; the isotropic energy fluence, $E_{\rm iso}$; the jet break time, $t_{\rm jet}$; and the redshift, z. In the concept we describe below, sensitive silicon and sodium iodide detectors mounted on a "Prompt Satellite" will establish $E_{\rm peak}$ and $E_{\rm iso}$, as well as burst location. A dedicated optical ground network will measure the redshift, z, as described in Appendix B. Compact X-ray Afterglow Telescopes (XATs), flying on two "Afterglow Satellites" will measure $t_{\rm jet}$. Figure A.1 depicts the interaction between the assembled assets for the mission concept.

The key to measuring $t_{\rm jet}$ and z is rapid and precise determination of astrometric positions, allowing the optical ground network and XATs to acquire the afterglow while it is still bright. Soft X-ray Camera (SXC) modules with 5 μm pixels on the Prompt Satellite designed for precision astrometry should be capable of locating bursts to an accuracy of $1''$-$3''$ in real time. This is sufficiently accurate for immediate ground-based IFS spectroscopy and for pointing a satellite-borne XAT with a narrow field of view.

The *HETE-2* SXC has selected a much higher yield of bright afterglows than other GRB locating instruments. In addition, the distribution of redshifts in this sample is very flat out to $z > 3$ (Berger et al. 2005). This is exactly the kind of sample that is required for a dark energy investigation.

Relative to the *HETE-2* SXC, the instrument concept we propose will cover a much greater solid angle with much higher operational efficiency. This broad coverage is the only way to acquire large numbers of bright bursts. The *HETE-2* SXC localizes $\sim$ 12 bright bursts/year in a $\sim$ 0.6 sr field of view with an operational efficiency of $\sim$ 20%. An array of *HETE-2* SXCs with hemispherical coverage and 80% operational efficiency would therefore localize $\sim$ 500 bright bursts/year. This is a very conservative lower limit on the burst rate for this instrument concept, which will have $\sim$ 30 times the detector area per solid angle and will therefore be far more sensitive than *HETE-2*. If the burst rate scales as $A^{1./3}$ (Doty 2004), this would imply that we might anticipate $\sim$ 1600 events per year. We adopt a conservative value of 800 per year.

The Prompt Satellite will also carry a large array of sodium iodide (NaI) scintillators to accurately measure burst spectra and fluences in the 5-1000 keV range. The technology for such detectors is well-established, based on their use in GRB satellites from the 1960s until the present–most recently in the Fregate instrument on *HETE-2*. Compared to Fregate, the proposed NaI array will provide 75 times larger area, 3 times greater solid angle, and 3 times greater observing time per year. Based on the Fregate rate of $\sim$ 90 bursts/year, we conservatively estimate that the Prompt Satellite will detect $\sim$ 1000 bright GRBs and XRFs per year–from which we can extract high S/N spectra for accurately measuring α, β, $E_{\rm peak}$, and the bolometric fluence over the 5-1000 keV range. The SXC silicon detectors will provide complementary spectra in the 1-10 keV range with the required sensitivity. In the following two appendices, we provide additional details on the space and ground segments of the mission concept, respectively.

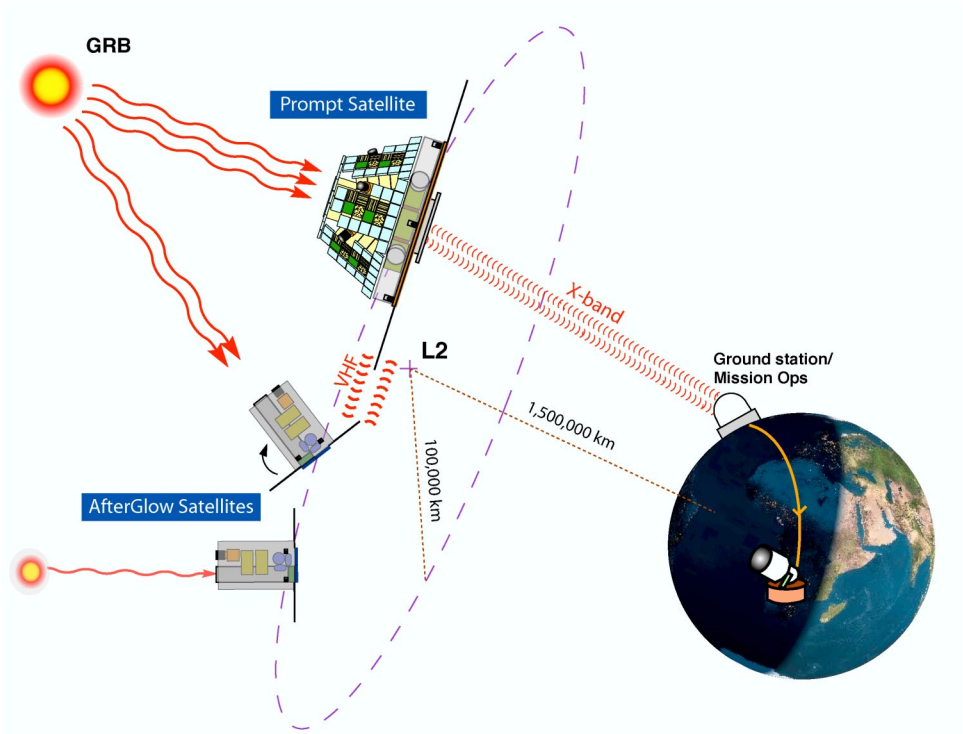

Fig. A.1.— Schematic diagram of spacecraft locations and operation.

A. Instrument Concept for Space-based Segment–GRB Satellites at L_2

A.1. Prompt Satellite

The Prompt Satellite is depicted in Figure A.2. From its location at L_2, the detectors on its seven facets view the sky continuously. Each facet contains 14 wide-angle ($\sim 140^\circ$ FOV) NaI detectors (1750 cm^2 area per facet), covering the 5-1000 keV energy range. Because the fields-of-view of the NaI detectors on adjacent facets overlap, it is possible to establish crude ($\sim 6^\circ$) localizations from detector counting rate ratios (as was done for the *BATSE* mission). Additional details on the NaI detectors are given in Table A.1.

To refine these crude localizations and to extend the X-ray energy range down to ∼1 keV, each facet also has eight large area Soft X-ray Cameras (SXCs) with X-ray CCD detectors (Table A.1). The eight detectors are equipped with different coded masks: 4 have one-dimensional masks (2 oriented in the X direction and 2 in the Y direction), 2 have two-dimensional masks, and 2 have no masks. The ensemble of eight SXC detectors works in concert to provide excellent burst detection sensitivities in the 1-15 keV band, as well as localization accuracy of 1.3″ in radius (90% C.L.).

The seven facets on the Prompt Satellite host 56 SXC cameras in total. Each of the 56 SXC cameras contains a wafer-scale (∼90 cm^2) CCD consisting of 16×16 panes with 1152 ×1152 pixels each. The multipane approach has many advantages. Each charge packet moves only a small distance (1.2 cm at most) to the readout, so that charge loss from radiation induced traps is minimized. Bad panes, caused by manufacturing defects or by micrometeorites that penetrate the camera entrance window, may be isolated and ignored: coded aperture imaging is insensitive to small gaps in focal plane coverage. Thus, a high manufacturing yield of acceptable wafers as well as a long detector life in orbit is assured. Each pane includes charge summation structures to make pixel summation fast and efficient. For the 1D modules, 576 rows are summed to produce a tall (2.9 mm) narrow (5 μm) effective pixel shape. For the 2D and open modules, the sums will be 24x24, for a 120 μm square effective pixel. This reduces the readout load from 19 billion pixels to 33 million. A 200 Mpix/s readout system will allow 4 Hz readout of the entire array of modules with allowance for overhead. Thus, the CCD detector time resolution is improved to 250 ms, 5 times better than for the *HETE-2* SXCs.

A large array of SXC modules requires a high performance data acquisition and processing system. We have previously investigated the design of such a system for a possible mission of opportunity. It appears practical, with technology available in 2005, to acquire and process X-ray CCD data for $\sim 1/60$ the power needed with *HETE* (1992) technology. *HETE-2* only provides $\sim$ 10W of power to support the SXC, but the larger spacecraft we envision should be able to provide at least 100W to the SXC array, so we anticipate a data acquisition and processing system with at least 600 times the *HETE-2* capacity supporting $\sim$ 200 times the silicon area. The extra capacity will provide better time resolution and better real time imaging. Additional details on the SXC camera and X-ray CCD detectors are given in Table A.3.

The sensitivity of the Prompt Satellite for establishing $E_{\rm peak}$ is depicted in Figure A.3. Both the scintillation detections ("DE NaI") and SXC cameras ("DE Si") are more than an order of magnitude more sensitive than flown on previ-

Table A.1: Scintillation Detectors for Prompt Satellite

Energy Range	5 - 1000 keV
Field of View	7 sr total
Number of Modules	$14 \times 7 = 98$
Scintillator	NaI(Tl)
Readout System	Photomultipliers (PMTs)
Sensitive Area	12,250 cm^2 ($14 \times 7 = 98$ units @ 125 cm^2)
Source Localization	6° (by projected area method)
Flux Sensitivity (10σ, 8-1000 keV)	10^{-8} ergs cm^{-2} s^{-1} (3× better than BATSE & Fregate)
Time Resolution	10 μs
Bright Burst Rate	$\sim$ 1000 per year (with measured $E_{\rm peak}$)
Flight Heritage	Fregate Instrument on *HETE-2*
Total Power	25 W
Total Mass	95 kg (50 kg Scintillators +40 kg PMTs +5 kg electronics)

ous missions.

Despite the large areas of the NaI and SXC instrument arrays, they are compact, low in mass, and require little power. As a result, the spacecraft power and mass resources are modest. We estimate that the Prompt Satellite (a "minisatellite") will require a net of < 300 W and < 400 kg, even allowing for ample reserves of 50% and 100%, respectively (Table A.3).

A.2. X-ray Afterglow Satellite

In Figure A.4, we show a concept for a microsatellite optimized to observe the X-ray afterglows. In Table A.4, we have compiled the power and mass resources needed for each of two such microsatellites. Even with a 100% reserve, each Afterglow Satellite requires only 60% of the mass of *HETE-2*. The power requirement per microsatellite is approximately 60% of the power requirement of *HETE-2*.

Each X-ray Afterglow Satellite will carry 9

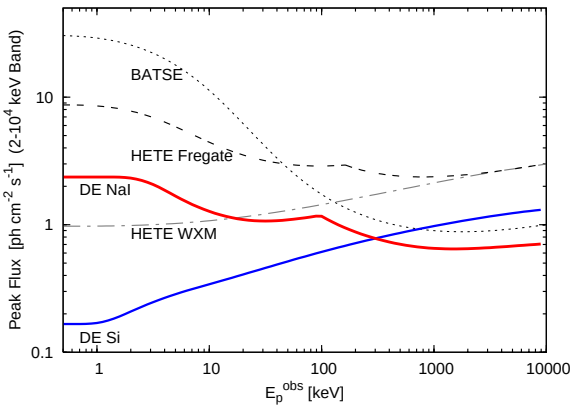

Fig. A.3.— The sensitivity curves for the Dark Energy Si and NaI detectors (colored lines) versus the observed GRB peak energy $E_{\rm peak}$. Also plotted are the sensitivities for BATSE (dotted black line) and *HETE-2* (dashed black and dot-dashed gray lines).

Table A.2: Silicon CCD Detectors for Prompt Satellite

Energy range	1-15 keV
Field of View	7 sr total (centered on anti-sun)
Module Configuration	1D cameras: 2 X, 2 Y
(on 1 of 7 satellite faces)	2D cameras: 2-D, 2 Open
CCD Detectors	Deep depletion silicon; 72K $\times$ 72K, with 5 μm pixels (Wafer scale device, segmented as $16 \times 16 = 256$ independent "panes", each with 1152×1152 pixels)
Pixel Summation	576×1 (1D) or 24×24 (2D)
Area per CCD	90 cm^2
Number of CCDs	8 CCDs/Face $\times$ 7 Faces = 56 CCDs
Total CCD Area	56 @ 90 cm^2 = 5040 cm^2
CCD Temperature	Passive cooling to -100C
Coded Mask Size	10 cm $\times$ 10 cm
Mask-to-Detector Separation	20 cm
Camera Resolution	10.3$''$for Nyquist sampling of mask pattern
Source Localization Accuracy (90% C.L.)	1.3$''$radius for 5σ detection in one XY pair (2 CCDs)
Flux Sensitivity (10σ, 2-10 keV)	1 s: 4.5×10^{-9} ergs cm^{-2} s^{-1}
	100 s: 4.5×10^{-10} ergs cm^{-2} s^{-1}
Time Resolution	250 ms
Bright Burst Localization Rate	$\sim$ 800 per year
Flight Heritage	X-ray CCDs on *ASCA*, *Chandra*, *HETE-2*, & *Astro-E*
Total Power	100 W
Total Mass	55 kg (40 kg cameras + 15 kg electronics)

(3×3) clustered, narrow field of view X-ray Afterglow Telescopes (XAT), each with its own CCD detector. The telescope and detector design parameters and performance statistics for a typical observation (field angle of 0.5$'$) are displayed in Table A.2. The XAT design is an updated version of the array of small telescopes flown and proven aboard the SAS-3 satellite in the mid-1970s (Hearn et al. 1976). The reflecting surface of each telescope is a paraboloid of rotation, coated with Ni. A single bounce at grazing incidence focuses 0.5 keV X-rays onto the CCD with excellent efficiency. (The efficiency at 2 keV declines by only a factor of 2 compared to its value near unity at 1 keV.) Each telescope is baffled to prevent X-ray's from field angles $> 1'$ from reaching the detector. The 9 telescope design is light (< 1 kg per telescope), and the small diameter (8 cm), thick-walled (3mm) unnested reflectors should be inexpensive to fabricate.

Each X-ray Afterglow Satellite will reach a limiting sensitivity of 2×10^{14} erg cm^{-2} s^{-1} in 4 ksec. We take this flux limit as a conservative estimate for the required sensitivity to detect late GRB jet break times. A flux $\sim 10\times$ greater was measured by the *Swift* XRT for GRB 050408 at

Table A.3: Resources for GRB Prompt Satellite

Item	Power (W)	Mass (kg)
X-ray CCDs (5,040 cm^2)	100	40 – Cameras
	–	15 – Electronics
Scintillation Detectors	25	50 – NaI
(12,250 cm^2)	–	40 – PMTs
	–	5 – Electronics
Attitude Control System	15	10
(Momentum wheels, Star trackers,		
Thrusters, Electronics)		
Command & Data Handling	5	5
(Electronics)		
Power System (Batteries, Converters	5	10
Solar panels)		
X-Band System	20	1
VHF System	4	1
Propellant (Cold gas)	–	5
Sums	174	182
Margin	87 (50%)	182 (100%)
TOTAL (w/ Margin)	261 W	364 kg

its jet break ($t \sim 5$ days) after $\gtrsim 10$ ksec of integration. Figure A.5 shows the sensitivity of an XAT (solid line) relative to the sensitivity of the *Swift* XRT (dotted line). For relatively bright sources (fluence $\gtrsim 2\times10^{-14}$ erg cm^{-2} s^{-1}), these small XAT instruments achieve the same signal-to-noise determination as does the *Swift* XRT, yet the required exposure is 2.5× shorter. For fainter sources, or for sources in crowded fields, the required exposure is $5-8\times$ shorter than for the *Swift* XRT due to the tighter PSF of the XAT (10.3″ HEW versus 18″ PSF[1]).

[1]http://www.swift.psu.edu/xrt/details

A.3. Launch Vehicle Requirements

As shown in Figure A.6, the Prompt Satellite and the two Afterglow Satellites are easily accommodated within the fairing of a Delta 7425, the same rocket used to launch the WMAP mission to L_2 (Bennett et al. 2003). Based on the mass estimates for the three satellites (Tables A.3 and A.4), the Delta 7425 launch mass capability to L_2 of 800 kg provides ample (>100% mass margin) for the MIDEX mission we envision.

A.4. Data Rate

The data handling strategy for our mission combines concepts from *RXTE* and *HETE-2*. An

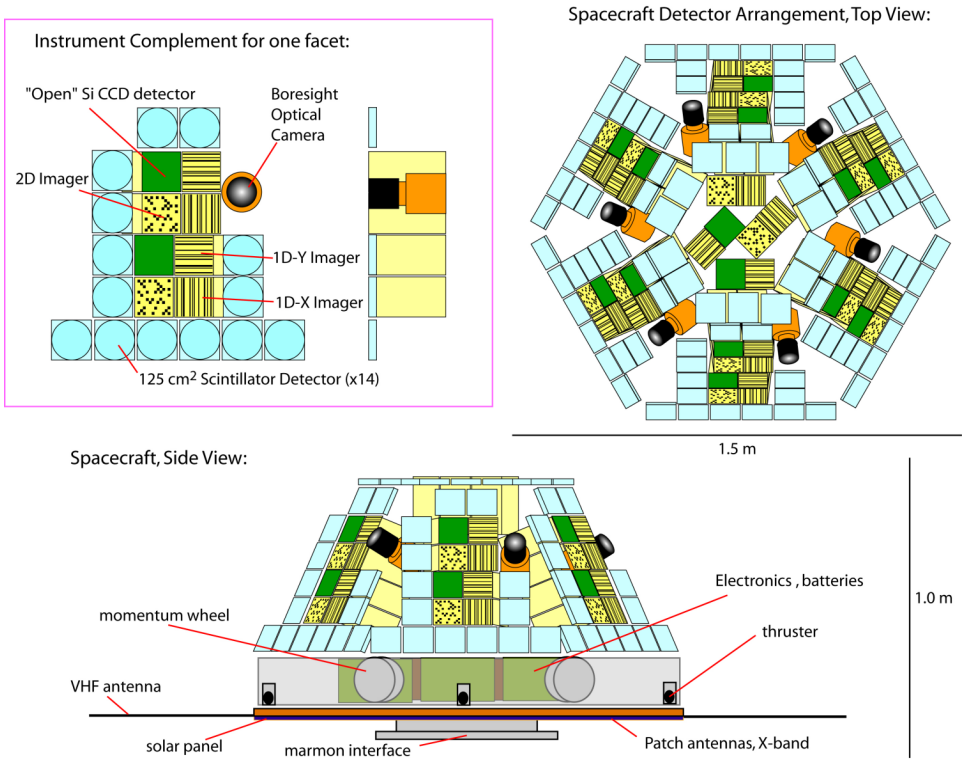

Fig. A.2.— Schematic diagram of the GRB Prompt Satellite.

RXTE-style bit code will represent raw event data from the scintillation detectors, with 32 channels of energy resolution and 20 ms time resolution. This code averages 2 bits/event. For the silicon detectors, the events are very sparse in the spatial/spectral/temporal resolution space. A run length encoding with 20 bits/event should be nearly optimal for these. The silicon detectors detect about an order of magnitude fewer photons than the scintillation detectors, so the total bit rates for the two detection systems are approximately equal.

Nearly all of the time, the diffuse X-ray background will dominate the event rate. A very intense burst may dominate the event rate for a few seconds, and a solar radiation storm may blind the detectors for awhile, but the diffuse X-ray rate determines the average raw data rate over time. For the encodings above, the average data rate is about 500 kbit/s. A 128 Gbit data store will therefore be able to hold ~ 3 days of data on board to support ground queries for more detail.

Because 500 kbit/s is much larger than our raw downlink rate of 30 kbit/s, we will need to be selective in what we send to Earth. We will bin the raw data from each face of the localization/spectra spacecraft into 16 channels with 1/4 second time resolution. With light data compression, this stream will be 3.6 kbit/s. This will constitute a standard survey data set. For most bursts, this should be sufficient to determine fluence and spectral parameters.

The imaging software on board will conduct a spatially resolved search for bursts: we will devote 2 kbit/s to the results of this search. The on board burst trigger algorithm will provide 1

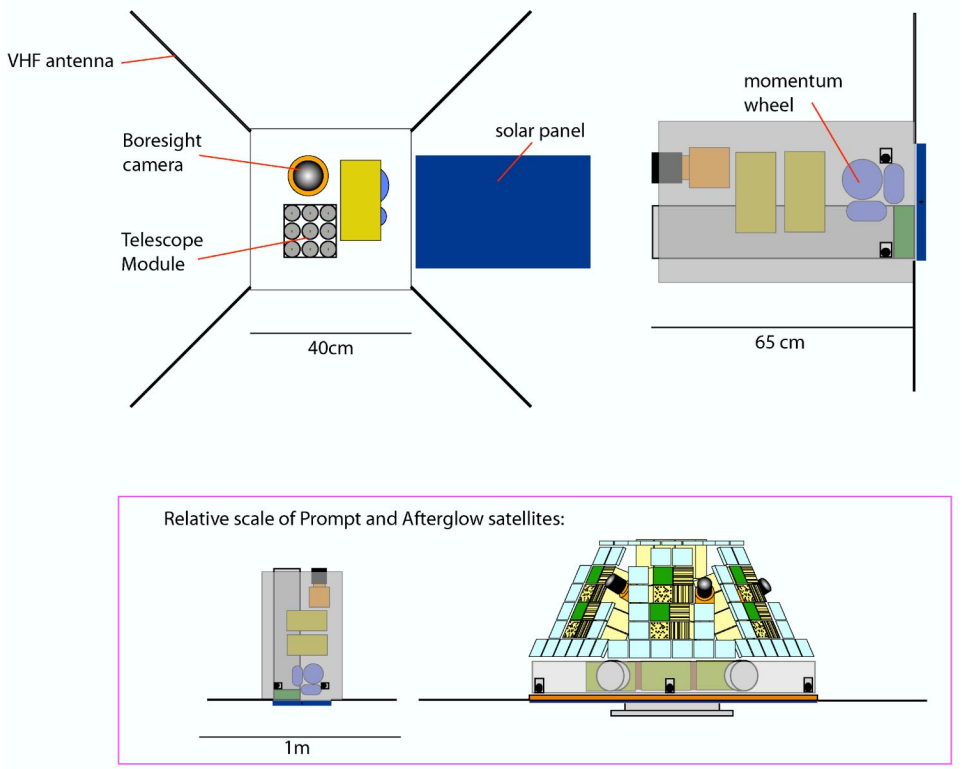

Fig. A.4.— Schematic diagram of Afterglow Satellite (1 of 2) with its X-ray Afterglow Telescope (XAT) array.

kbit/s of diagnostic information. Each of the two Afterglow Satellites will send 600 bit/s to the Prompt Satellite for relay to Earth.

The above, plus spacecraft housekeeping and data overhead, will use 10 kbit/s, or 1/3 of the available downlink. The other 2/3 will be used to respond to ground queries for more detail. In most cases, we expect that all of the event data from a burst will be requested. For the brightest/longest bursts, an *RXTE*-like binning and recoding engine will reduce the data mass to a manageable amount.

For the afterglow satellites, 10 photon event/s will yield 320 bit/s. The remaining 280 bit/s will be housekeeping and overhead. In most cases the afterglow intensity will be much less than 1 photon/s at the jet break time so this should provide adequate dynamic range.

A.5. Navigation and Station-Keeping

For simplicity, the Delta 7425 payload bus will transport the "mother" mini spacecraft (aka Prompt Satellite) and the accompanying two "daughter" micro spacecraft (aka Afterglow Satellites) to the vicinity of the Earth-Sun L_2 Lagrangian point where they will be injected into a so-called halo (or Lissajous) orbit of *ca.* 100,000-200,000 km radius. Such orbits (Farquhar 1970) lie close to a plane oriented at $\sim 72^\circ$ from the ecliptic. Once a halo orbit has been achieved, the daughter spacecraft will separate at low relative velocities so as to execute Lissajous orbits

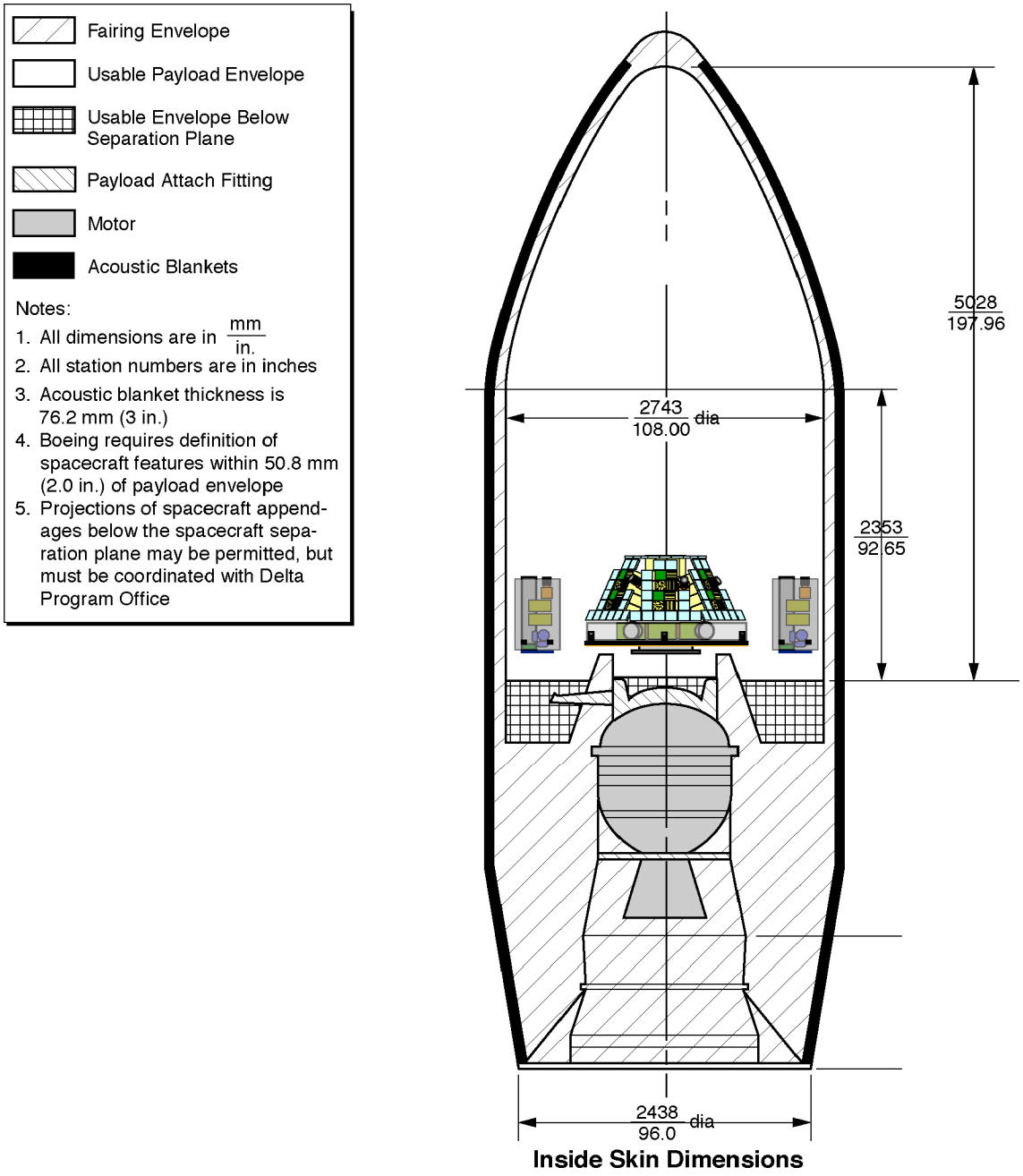

Fig. A.6.— Schematic diagram of the GRB Prompt Satellite and 2 GRB Afterglow Satellites in the Delta 7425 rocket faring. There is ample clearance for the 3 small satellites to fit within the faring. Since the Delta 7425 can launch 800 kg to L_2, it can easily launch the combined payload mass (see Tables A.3 and A.4), even with a mass reserve of more than 100%.

Table A.4: Resources for Afterglow Satellites (per Satellite)

Item	Power (W)	Mass (kg)
CCD Detectors	1	2
Telescope Array	–	10
Attitude Control System (Momentum wheels, Star trackers, Thrusters, Electronics)	15	10
Command & Data Handling (Electronics)	5	5
Power System (Batteries, Converters, Solar panels)	4	8
VHF System	4	1
Propellant (Cold gas)	–	2
Sums	29	38
Margin	14.5 (50%)	38 (100%)
TOTAL (w/ Margins)	44 W	76 kg

(Barden & Howell 1998) relative to the mother spacecraft. None of the spacecraft will be in stable orbits—they will separate from each other, and from the vicinity of the L_2 point, along an "unstable manifold" of the halo orbit at an exponentially increasing rate unless appropriate velocity corrections are made. The mother spacecraft will contain an X-band transceiver, synchronous transponder, and high-gain antenna, allowing it to be tracked directly from Earth—utilizing round-trip time delay measurements to determine range, and two-way Doppler tracking to measure line-of-sight velocity, right ascension, and declination. Daily tracking as part of science data acquisition contacts at ∼100 m accuracy will be sufficient to permit velocity corrections to be computed and executed to maintain the halo orbit with low fuel consumption and slow drift orthogonal to the orbit plane (Collange & Leitner 2004). Since the total delta-V requirements will be < 5 m s^{-1} yr^{-1} (Farquhar & Dunham 1990), a small cold gas system (< 5 kg propellant for the mother-sat, <2 kg propellant for each of the daughter-sats) will suffice for the nominal 2 year mission. We propose the use of a simple low-gain phased-array antenna on the daughter spacecraft to determine the direction to the mother spacecraft with the VHF uplink; 4-6 whip antennas at different places on the spacecraft body will feed a coherent multichannel digital receiver. The phase difference between the antennas will indicate the direction of the mother spacecraft. (With antennae separated by less than a wavelength this is more like classic 1940's radio direction finding than a 21st century phased array, but it should suffice for our requirements.) This knowledge may also be used to phase the antennas for maximum satellite-to-satellite link margin. The daughter spacecraft will relay their data through the mother space-

Table A.5: X-ray Afterglow Telescope (XAT) Design Parameters

Focal Length (F)	80cm
Mirror Length	60cm
Mirror Outer Diam.	8cm ($F/10$)
Mirror Thickness	3mm
Number of Telescopes per Satellite	9
Mass per Telescope	0.9 kg
Telescope PSF	10.3″HEW, 0.5 keV
Effective Area	286 cm^2, 0.5 keV
Detection Element	5x5 micron pixel
Pixel Scale	1.3″/pixel
Field of View (radius)	60 arc second
Sensitivity (in 4 ksec)	2×10^{-14} erg/cm/s

Table A.6: X-band Downlink Budget

Data type	kbit/s
Afterglow data relay	1.2
GRB Survey	3.6
Soft imaging search	2.0
Trigger status	1.0
Housekeeping	1.0
Overhead	1.2
Detailed analysis	20.0
TOTAL	30.0

craft, and cannot therefore be reliably tracked from the Earth. Instead, their range, range rate, and bearing from the mother spacecraft will be determined using their VHF (2-meter, 140 MHz) transceivers. Each daughter will possess a single dipole antenna, a VHF transceiver, and a synchronous transponder, whereas the mother will employ a 3 dimensional antenna array, *e.g.,* simple 1/4-wave VHF dipoles at each apex of an equilateral pyramid, each with its own receiver. The physical antenna can be spring-deployed (tape measure) elements of the type used on the *HETE* satellite, for which the VHF antenna was literally a $\sim$ 50 cm long spring tape measure that uncoiled in orbit. The mother spacecraft will transmit on a single dipole and its receiver outputs will be heterodyned to baseband and cross-correllated to extract the relative phase delay ($\pm10^{-3}$ rad) of each baseline. Since the antenna spacing is comparable to the carrier wavelength, aliasing will not occur and the direction from the mother to each daughter will be determined to $\sim$1 milliradian accuracy. Combined with traditional VHF ranging and range-rate extraction, the relative location of each spacecraft can be estimated, and velocity corrections can be computed to maintain each daughter in the vicinity of the mother.

A.6. Satellite Telecommunication

The constellation of GRB Prompt ("mother") and two Afterglow ("daughter") Satellites will circle about L_2 in a halo orbit, of radius 100,000-200,000 km. All ground communication will pass through the Prompt Satellite over an X-band (10 GHz) link, utilizing two small ($\sim$ 2000 cm^2), flat phased array antennae on the sun- (and earth-) facing surface. The phased array antennae will permit continuous communication to earth without requiring a steerable dish or a re-orientation of the Prompt Satellite, which would disrupt GRB science data collection. The beam of the phased array antennae will be sufficiently narrow ($< 2^\circ$) to avoid interference from solar RFI, yet broad enough to illuminate the entire earth (viewed from the L_2 halo orbit, the earth subtends $\sim 0.5^\circ$ and is offset $\sim 4^\circ$ from the sun). In addition, the Prompt Satellite will communicate with the Af-

Table A.7: X-band Telemetry Link Margins for a 5m Diameter Ground-Based Antenna

X-band Prompt Satellite-to-Ground	
Eb/N at 1e-6:	7.6dB
Modulation:	BPSK+1/2Viterbi
Spectrum utilization:	0.5
Spacecraft TX power:	5W
Distance:	1,504,0000 km
Bit rate:	30 kbps
Link margin:	4.13 dB
X-band Ground-to-Prompt Satellite	
Eb/No at 1e-6:	14.2
Modulation:	CPFSK
Spectrum utilization:	1
Ground station TX power:	50W
Bit rate:	113,600 bps
Link margin:	5.20 dB

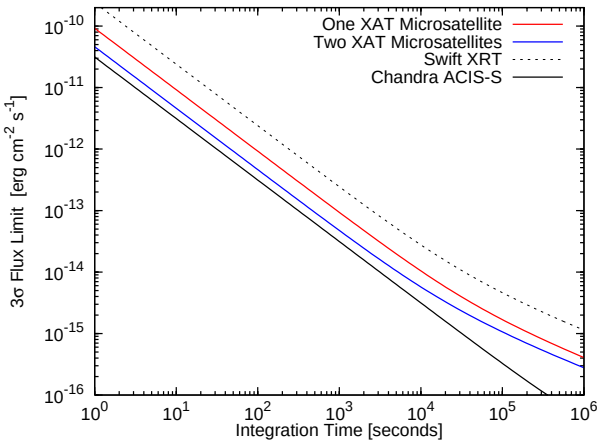

Fig. A.5.— The XAT sensitivity (colored lines) versus exposure time. The red line refers to a single XAT microsatellite viewing a given source, while the blue line refers to both XAT microsatellites simultaneously viewing the same source. Also plotted is the sensitivity for the *Swift* XRT (dotted line) and for *Chandra* ACIS-S (heavy black line).

terglow Satellites via 2-way VHF link.

Table A.8: VHF Telemetry Link Margins

VHF Satellite-to-Satellite	
Frequency:	137.96 MHz
Spacecraft TX power:	1 W
Bit rate:	600 bps
Link margin	27 dB @ 10^3 km
(@ satellite-to-satellite	7 dB @ 10^4 km
distance)	

The VHF transceiver system described in "Navigation and Station-Keeping" will also serve to transmit the GRB burst alerts and $\sim$ arcsecond localizations from the Prompt Satellite to the Afterglow Satellites. (An automated scheduler on the Prompt Satellite will establish which of the two Afterglow satellites will be assigned to a given alert.) In addition, the VHF link will

be utilized to transfer the X-ray afterglow observation data from the Afterglow Satellites back to the Prompt Satellite, for re-transmission to earth. We estimate that the satellite-to-satellite separations can be easily maintained to <1000 km, even if the station-keeping thruster events are only scheduled a couple of times per month. To assess the link requirements for this VHF system, we have scaled from the measured properties of the *HETE* VHF burst alert system. (NB: Although *HETE* is is low earth orbit and communicates to ground receivers, the link distances are typically 1000-2000 km, which is comparable to the satellite-to-satellite distances near L_2 that we are considering. Furthermore, the VHF RFI environment is much more favorable at L_2, since VHF RFI is dominantly terrestrial in origin.)

B. Instrument Concept for Ground-Based Segment – Dedicated Telescope Network

B.1. Integral Field Spectrometer-equipped Telescopes

A 2.4-meter Ritchey-Chretien telescope (such as production units from EOST[2]) will provide a small 30 arcsecond diameter field of view to an lenslet array coupled to optical fibers. An off-the-shelf 2.4m telescope should be able to slew and set to 3 arcsecond accuracy. Focus and pointing will be monitored by pointing to a table of known standard stars during clear night operations.

The lenslet array will be a set of hexagonal elements, each subtending 0.5 square arcseconds (approx 0.7″ on a side). We require 800 lenslets to cover a square 20″x20″spectroscopic FOV at Cassegrain focus. The output of the fibers will feed a double-spectrograph, similar in design to the SDSS grism spectrographs. The fibers will be aligned and collimated to provide an average of 5 pixel separation between individual spectra, and 2000 pixels on each blue and red side (4000 pixels total in each spectrum, with minimal overlap near the dichroic).

Table B.1: Sensitivity Estimate for Spectrgraphic Redshift Limits for Ground-Based IFS-equipped Telescopes

m_{AB}	Bright Sky S/N 19 mag/arcsec^2	Dark Sky S/N 21 mag/arcsec^2
16.0	75.3	78.9
17.0	43.4	48.2
18.0	23.0	28.2
19.0	11.0	15.4
20.0	4.8	7.6
21.0	2.0	3.4

If we assume pixels which are approximately 100 km/s in dispersion, and an effective aperture of 1.0 m^2 (25% end-to-end efficiency) then a single 900 second exposure will yield approximately the S/N values given in Table B.1 for two extremes in sky conditions.

The spectrographs will have complete wavelength coverage from 3100-9600 Angstroms. This covers the absorption line doublet of MgII over the full redshift range of $0.11 < z < 2.4$. In addition, it will cover the CIV doublet absorption from $1.0 < z < 5.0$, and Damped Lyman-α absorption from $1.6 < z < 6.5$.

To detect MgII and CIV robustly, one would require an approximate S/N of 5 per pixel. So in dark-sky and bright-sky (3/4 moon) conditions, a single 900 second exposure is sufficient down

[2]http://www.eostech.com/two_point_four_meter.php

Table B.2: Budget Breakdown for Dedicated Support Telescope & IFS Instrument Configuration

\$2.0M	2.4 meter automated telescope: built,tested and delivered
\$1.5M	Optical double-sided spectrograph with fiber/lenslet array.
\$0.3M	Estimate for site lease and minimal observatory support over 2 years.
\$1.0M	Data reduction, z determination and quick response support over the 2 year mission.
\$4.8M	TOTAL per site

to $m_{AB} = 20$th magnitude. To accurately detect these MgII and CIV redshifts down to m_{AB}=21 will require 90 minutes of exposure in bright time and 30 minutes in dark lunar conditions (see Table B.1). The Damped Lyman-alpha feature is much easier to detect, and should be recovered in any spectra with S/N > 2.0 per pixel.

To have complete sky coverage, we would require 5 or 6 identical telescopes adequately separated in longitude. Candidate sites include: Canary Islands, Chile, Southwestern USA, Hawaii, Australia, and Southern Africa. Each of the telescopes would be built at an established astronomical site with good infrastructure. Although the telescopes will be designed to run autonomously, lost observing time could be minimized if observatory staff could respond in a reasonable time if trouble arose. In Table B.2, we give the estimated costs per dedicated observatory site for a two year mission. Since the total is \$4.8M per site, establishing 6 sites would require ∼\$30M, which would comprise ∼10% of the total budget for the MIDEX mission.

REFERENCES

Barden, B. T., & Howell, K. C., 1998, AAS 98

Bennett, C. L., et al. 2003, ApJ, 583, 1

Berger, E., et al., 2005, astro-ph/0505107

Collange G., & Leitner, J., 2004, AIAA 2004-4781, Providence, 16-19 August

Doty, J. 2004, AIP Conf. Proc. 727, 708

Farquhar, R. W. 1970, NASA technical report, R-346

Farquhar, R. W., & Dunham, D. W. 1990, Observatories in Earth Orbit and Beyond, Y. Kondo, ed., Klewer Academic Publishers, 1990, p 391

Hearn, D. R., et al. 1976, ApJ, 203, L21